ARTICLES
https://doi.org/10.1038/s41551-019-0435-y

nature biomedical engineering

Bioresorbable photonic devices for the spectroscopic characterization of physiological status and neural activity

Wubin Bai[1,2,20], Jiho Shin[3,20], Ruxing Fu[4,20], Irawati Kandela[5,6], Di Lu[1,2], Xiaoyue Ni[1,2], Yoonseok Park[1,2], Zhonghe Liu[7], Tao Hang[8], Di Wu[2,9], Yonghao Liu[7], Chad R. Haney[6,10], Iwona Stepien[5,6], Quansan Yang[2,11], Jie Zhao[1,2], Khizar Rehan Nandoliya[12], Hao Zhang[1,2,13], Xing Sheng[14], Lan Yin[4], Keith MacRenaris[6,10], Anlil Brikha[6,10], Fraser Aird[5,6], Maryam Pezhouh[15], Jessica Hornick[16], Weidong Zhou[7] and John A. Rogers[1,2,9,11,12,17,18,19]*

Capabilities in real-time monitoring of internal physiological processes could inform pharmacological drug-delivery schedules, surgical intervention procedures and the management of recovery and rehabilitation. Current methods rely on external imaging techniques or implantable sensors, without the ability to provide continuous information over clinically relevant timescales, and/or with requirements in surgical procedures with associated costs and risks. Here, we describe injectable classes of photonic devices, made entirely of materials that naturally resorb and undergo clearance from the body after a controlled operational lifetime, for the spectroscopic characterization of targeted tissues and biofluids. As an example application, we show that the devices can be used for the continuous monitoring of cerebral temperature, oxygenation and neural activity in freely moving mice. These types of devices should prove useful in fundamental studies of disease pathology, in neuroscience research, in surgical procedures and in monitoring of recovery from injury or illness.

Understanding metabolic and physiological pathways associated with critical diseases is essential in providing target-specific, timely and effective therapeutic treatments[1–3]. Measurements of local changes in these pathways can serve as the basis for optimized pharmacological delivery schedules, surgical intervention procedures and recovery/rehabilitation protocols[4–6]. Functional magnetic resonance imaging, near-infrared spectroscopy, magnetoencephalography and positron emission tomography techniques offer powerful capabilities for monitoring internal body processes in such contexts, but they cannot provide continuous measurements over timeframes that can range from days to months or more. Traditional electronic implants can be considered, but they require subsequent surgical extraction to eliminate unnecessary device loads on (and associated health risks to) the patient[7–9].

In comparison, bioresorbable electronic technologies offer unique opportunities whereby diagnosis and therapy can occur continuously at targeted depths inside the body for well-defined, finite time periods matched to those of the treatment and recovery processes. Complete bioresorption into benign end products that clear through natural body mechanisms eliminates the hardware without the need for secondary surgeries[10–16]. Recent examples include: bioresorbable electronic sensors to track intracranial pressure[11] and to spatiotemporally map electrical activity from the cerebral cortex and cardiac muscle tissue[17,18]; devices to apply controlled therapy for endovascular diseases[19]; and platforms to affect infection abatement[12]. As a complement to electronic sensing modalities, spectroscopic measurements at visible and near-infrared wavelengths can reveal physical and chemical properties of biological tissues, thereby providing a strategy for monitoring vital biochemical processes and sensing key physiological parameters[20–23]. Here, we report materials, device architectures, performance attributes, biocompatibility assessments and in vivo demonstrations of multifunctional bioresorbable devices for spectral characterization of biotissues and biofluids. The presented designs allow for minimally invasive implantation via an injection process, with a construction in which all constituent materials naturally resorb via hydrolysis followed by metabolic clearance after a well-defined operational time. The technology enables continuous monitoring of critical

[1]Department of Materials Science and Engineering, Northwestern University, Evanston, IL, USA. [2]Center for Bio-Integrated Electronics, Northwestern University, Evanston, IL, USA. [3]Department of Chemical and Biomolecular Engineering, University of Illinois Urbana–Champaign, Urbana, IL, USA. [4]School of Materials Science and Engineering, Tsinghua University, Beijing, China. [5]Center for Developmental Therapeutics, Northwestern University, Evanston, IL, USA. [6]Chemistry Life Processes Institute, Northwestern University, Evanston, IL, USA. [7]Department of Electrical Engineering, University of Texas at Arlington, Arlington, TX, USA. [8]State Key Laboratory of Metal Matrix Composites, School of Materials Science and Engineering, Shanghai Jiao Tong University, Shanghai, China. [9]Department of Biomedical Engineering, Northwestern University, Evanston, IL, USA. [10]Center For Advanced Molecular Imaging, Northwestern University, Evanston, IL, USA. [11]Department of Mechanical Engineering, Northwestern University, Evanston, IL, USA. [12]Department of Chemistry, Northwestern University, Evanston, IL, USA. [13]Department of Chemistry, Key Laboratory of Bioorganic Phosphorus Chemistry & Chemical Biology, Tsinghua University, Beijing, China. [14]Department of Electronic Engineering, Tsinghua University, Beijing, China. [15]Northwestern Medicine, Feinberg School of Medicine, Northwestern University, Evanston, IL, USA. [16]Biological Imaging Facility, Northwestern University, Evanston, IL, USA. [17]Department of Neurological Surgery, Northwestern University, Evanston, IL, USA. [18]Department of Electrical and Computer Engineering, Northwestern University, Evanston, IL, USA. [19]Simpson Querrey Institute for BioNanotechnology, Northwestern University, Evanston, IL, USA. [20]These authors contributed equally: Wubin Bai, Jiho Shin, Ruxing Fu. *e-mail: jrogers@northwestern.edu

physiological parameters such as tissue oxygenation, temperature and neural activity for local information on tissue health and metabolic activity[24]. The devices incorporate a collection of bioresorbable optical components including: single-junction photodetectors based on nanomembranes of device-grade monocrystalline silicon (Si nanomembranes); foundry-produced tri-colour photodetectors based on tri-layer stacks of Si P–N junctions; optical multilayer filters of SiO_x and SiN_y; and optical fibres of poly(lactic-*co*-glycolic acid) (PLGA). System-level demonstrations include devices that inject into deep brain regions of freely moving mice for continuous absorption spectroscopic analysis of biochemical and physiological status. Systematic in vitro and in vivo studies establish the feasibility and accuracy of the devices in monitoring cerebral oxygenation, neural activity and temperature. Studies of biodistribution, blood chemistry and complete blood count highlight processes by which these technologies undergo bioresorption.

Results and discussion

Configuring the devices into shapes that resemble hypodermic needles, with dimensions around 600 µm wide and 160 µm thick, facilitates minimally invasive implantation (Fig. 1a). The active sensing region (Fig. 1b,c), supported on a substrate of PLGA (thickness: 10 µm), consists of three key components: (1) a bioresorbable fibre (diameter: ~150 µm) made of PLGA (refractive index: ~1.50) for delivering light of a certain wavelength to the sensing probe; (2) a bioresorbable photodetector made from a nanomembrane of doped monocrystalline Si (thickness: 1,500 nm) for generating electrical signals in response to transmitted light; and (3) electrodes made of thin films of zinc (Zn) (thickness: 400 nm) for electrical readout. A thin layer of SiO_2 (thickness: ~50 nm; refractive index: ~1.45; Fig. 1b) separates the PLGA fibre from the substrate to enhance light confinement inside the fibre, and to encapsulate, for a controlled period of time[25], the electrical components (photodetectors and Zn electrodes). The photodetector uses comb-like geometries (Fig. 1d) for both *p*- and *n*-doped regions to maximize the area coverage of the depletion region and to enhance the overall quantum efficiency (Supplementary Table 1). The measured current–voltage (*I*–*V*) curves in the dark and during illumination with green (wavelength: 530 nm), red (wavelength: 633 nm) and white light (broad-band wavelength) show excellent rectifying behaviour (Fig. 1e), with a dark current of 4.97×10^{-2} nA, responsivities of 0.135 and 0.133 A W^{-1} for green and red light, respectively, and quantum efficiencies of 31.5 and 26% for light at these wavelengths, respectively (Supplementary Table 1). The photocurrent density exhibits a linear response with optical power density, examined at red (633 nm) and near-infrared (850 nm) wavelengths (Fig. 1f). The photocurrent as a function of time under time-modulated illumination (rectangular temporal waveform, using light at a wavelength of 633 nm; Fig. 1h) shows response times of <0.1 s with no observable overshoot or oscillation.

Another key component—the biodegradable fibre—results from a simple drawing process applied to a bulk preform heated to 200 °C on a hotplate to yield a PLGA core (Supplementary Fig. 1a)[26]. Using the tip of a commercial fibre as a lead for the fibre-drawing process directly couples the resulting bioresorbable fibre to the commercial fibre (Supplementary Fig. 18). Dipping into sodium alginate solution (2 wt%) forms a uniform coating of a bioresorbable hydrogel (alginate) that serves as a cladding (Supplementary Fig. 1a). Immersion into a calcium chloride solution (0.5 wt%) ionically crosslinks the alginate to complete the fabrication (Supplementary Fig. 1 and Supplementary Note I show that the optically improved performance can be achieved using multiple cladding layers, which include a 200-nm-thick sputtered SiO_2 and alginate hydrogel (Supplementary Fig. 19)). Connecting the bioresorbable optical probe through a commercial fibre (diameter: 1 mm) to an external tunable laser source (an NKT Photonics SuperK COMPACT supercontinuum laser coupled with a SuperK VARIA tunable single-line filter; tuning range wavelength: 400–840 nm; wavelength accuracy: ±5 nm), and through two wires (diameter: 80 µm), to an external data acquisition system prepares the system for implantation and operation, with little constraint on the freedom of movement during continuous physiological monitoring in awake animal models (Supplementary Figs. 2 and 13).

An essential feature of the implanted components is that the constituent materials (Si, Zn, SiO_2 and PLGA) are entirely bioresorbable by dissolution reactions in biofluids to yield benign end products including H_4SiO_4, $Zn(OH)_2$, lactide and glycolide, which can be further metabolized and cleared by the body[25,27–30]. Figure 1h,i and Supplementary Fig. 3 characterize the dissolution behaviour of the key components (bioresorbable photodetector and bioresorbable fibre) individually, both in vitro and in vivo. Figure 1h and Supplementary Fig. 3a,b show the measured *I*–*V* curves in the dark and during illumination with white light, and the corresponding optical images of a bioresorbable photodetector at various stages after immersion in phosphate buffered saline (PBS) at 37 °C. The thin SiO_2 encapsulation layer effectively prevents water from penetrating into the active sensing area for the first 2 d. Slopes of these curves gradually decrease with time in forward bias mode, mostly due to hydrolysis of the Si nanomembrane and the Zn electrodes. On day 9, dissolution-induced fracture of the Zn electrodes creates an electrical open that leads to zero measurable photocurrent (Fig. 1h and Supplementary Fig. 3a,b). Immersion of a film of Zn (thickness 1 µm, deposited by electron beam evaporation) in a reservoir of PBS (with a replacement rate of 10 vol.% d^{-1}) at 37 °C reveals that the hydrolysis process leads to fragmentation that yields platelets composed mainly of $Zn(OH)_2$, with some amount of ZnO and Zn, as observed on day 3 (platelet lateral dimensions: ~75–150 µm; Supplementary Fig. 4). The sizes of these platelets decrease with time to dimensions of ~250 nm on day 10. The computed X-ray tomography images in Fig. 1i show the gradual disappearance of an array of bioresorbable photodetectors (the layout appears in Supplementary Fig. 5) implanted in the subcutaneous region near the flank of a mouse model. On day 45, the array is invisible under computed tomography, consistent with complete bioresorption (Fig. 1i). Supplementary Fig. 3c,d shows the dissolution behaviour of the PLGA fibre, indicating an initial swelling on day 1 and a gradual dissolution within 2 weeks in PBS at 37 °C. The optical transmission decreases dramatically on day 3 and eventually become undetectable on day 20.

Basic capabilities in spectroscopic characterization[31] can be realized using a tri-colour bioresorbable Si photodetector (Fig. 2) or a set of bioresorbable optical filters (Fig. 3). Figure 2a presents a schematic (with an exploded view on the right) of the former type of device, which consists of four doped layers (from top to bottom: layers A, B, C and D correspond to *n*-, *p*-, *n*- and *p*-doped layers, respectively, with the doping concentrations and thicknesses shown in Supplementary Table 2) vertically aligned together to form three junctions: AB, BC and CD, respectively[32]. Perspective images (Fig. 2b) generated by optical profilometry and tilted-view scanning electron microscope (SEM) images (Supplementary Fig. 6a,b) highlight the results of etching steps to expose each doped layer (layers A, B, C and D) for metal contacts (as shown in Supplementary Fig. 6c). Coupling this tri-colour photodetector to a PLGA fibre for light delivery and four Zn metal electrodes for electric readout yields a simple, bioresorbable spectrometer (Fig. 2c). Figure 2d shows *I*–*V* curves (in a dark environment) for junctions AB, BC and CD, respectively, indicating excellent rectifying behaviours, with dark currents of 3.24×10^{-2}, 1.52×10^{-1} and 9.87×10^{-3} µA, respectively, and responsivities of 0.15, 0.15 and 0.11, respectively (the measured *I*–*V* curves for junctions AC, BD and AD appear in Supplementary Fig. 6d). The penetration depth of light (wavelengths between 400 and 1,000 nm) in Si increases with wavelength, thereby enabling peak responsivities for junctions AB, BC and CD at wavelengths of 490, 570 and 720 nm, respectively (Fig. 2e). Figure 2f

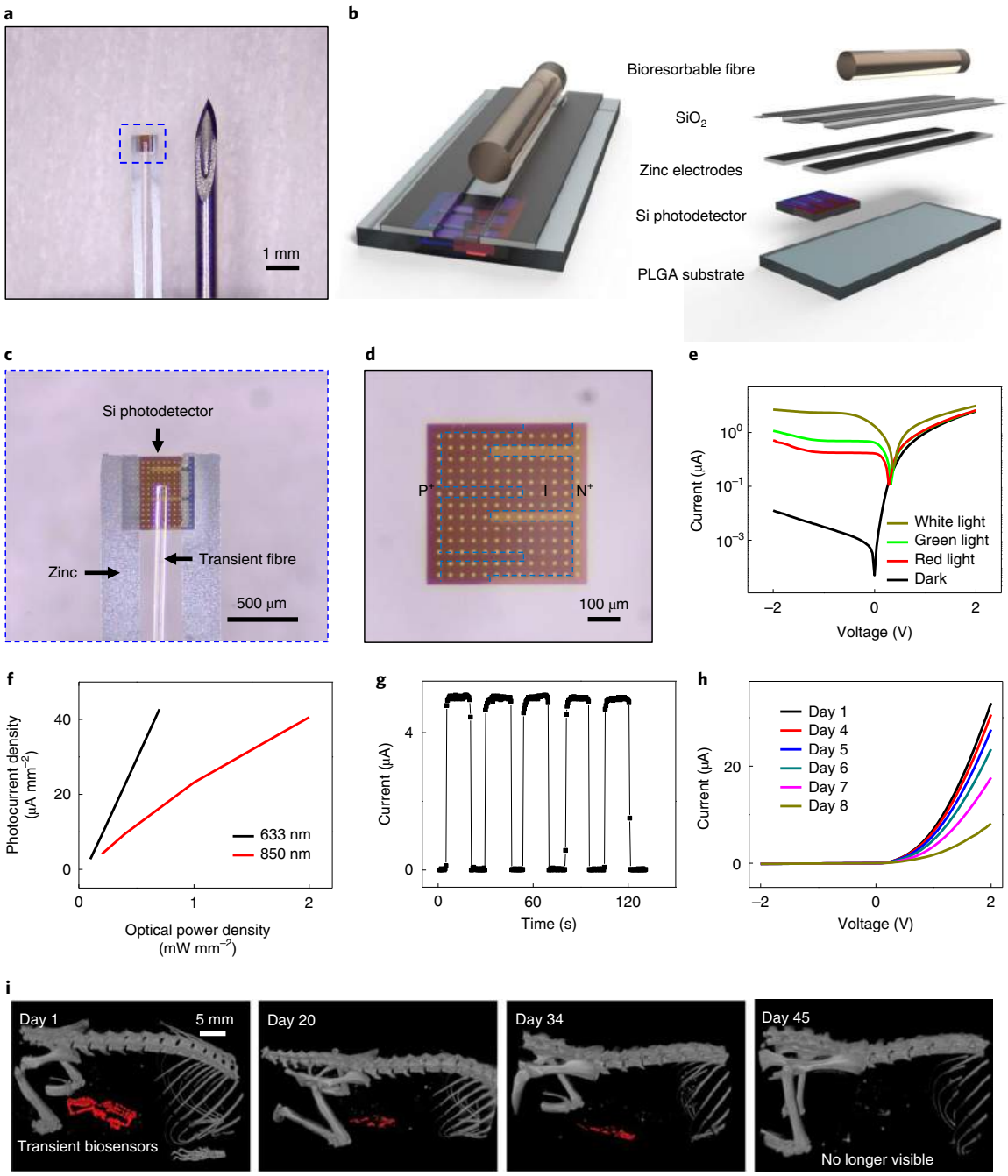

Fig. 1 | Bioresorbable Si photodetector with a bioresorbable fibre optic probe for spectroscopic characterization of biological tissues. a, Optical microscope image of a bioresorbable spectrometer based on an Si nanomembrane photodetector and a bioresorbable fibre optic probe, placed next to the tip of a hypodermic needle (diameter: 650 μm). The device consists of: a photodetector constructed from a 1,500-nm-thick Si nanomembrane; two Zn electrodes (thickness: 400 nm; width: 200 μm); a bioresorbable optical fibre (made from PLGA; diameter: 150 μm); and a supporting substrate made from PLGA (thickness: 10 μm). **b**, Schematic of the device, with an exploded view shown to the right. **c**, Enlarged view of the active sensing region. **d**, Optical image of a fully bioresorbable PIN photodetector constructed with a 1,500-nm-thick Si nanomembrane. Dashed blue lines define the *n*-type, *p*-type and intrinsic regions. **e**, Measured *I*–*V* characteristics of the device under illumination with white light (broad-band wavelength), red light (wavelength: 633 nm) and green light (wavelength: 530 nm), and in a dark environment. **f**, Measured photocurrent density as a function of optical power density for illumination with red (wavelength: 633 nm) and near-infrared light (wavelength: 850 nm). **g**, Measured photocurrent as a function of time for illumination with light after passing through a chopper (red light, wavelength: 633 nm; optical power: 4 mW). **h**, Measured *I*–*V* characteristics (in a dark environment) at various times after immersion in PBS at 37 °C. **i**, Three-dimensional-rendered computed tomography images of mice collected over 7 weeks after the implantation of arrays of bioresorbable Si nanomembrane photodetectors (as shown in Supplementary Fig. 4). The images indicate the gradual disappearance of the devices, which eventually became invisible under computed tomography on day 45. In **e**–**h**, $n = 6$ independent experiments. In **i**, $n = 3$ biologically independent mice.

shows measured photovoltages generated from junctions AB, BC and CD in response to illumination using white light (broad-band wavelength) after passing through a chopper, indicating a response time for all three junctions that is <0.05 s. As the colour content of the illumination changes, the signals generated from the three junctions change accordingly, in a way that reflects the variations

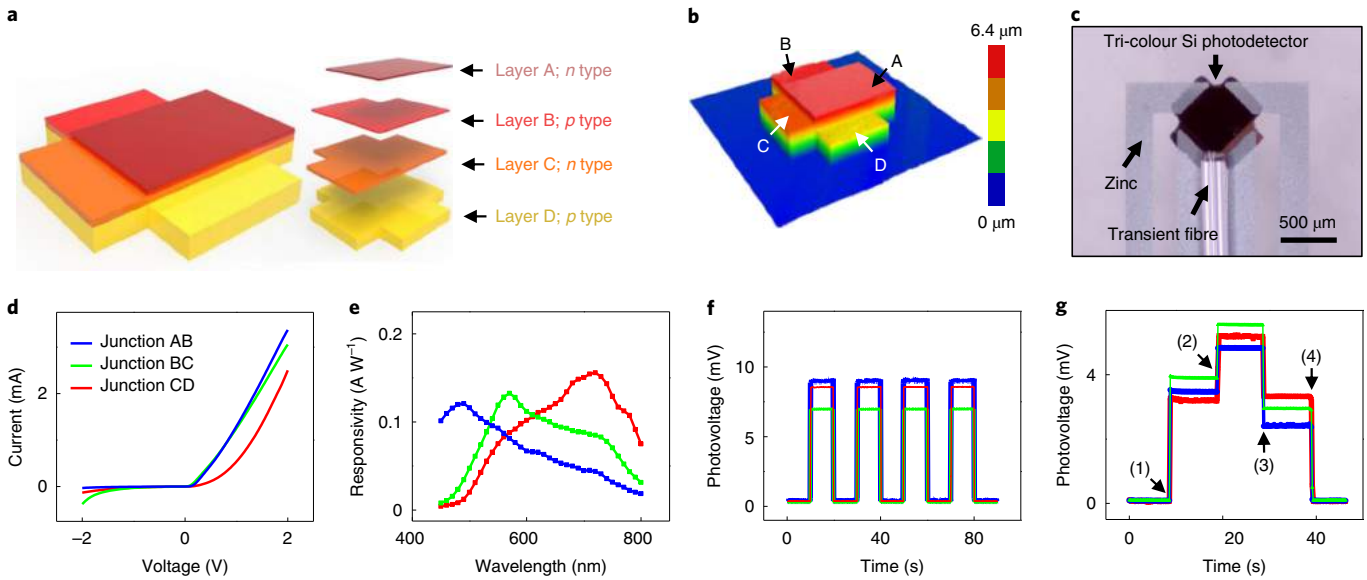

Fig. 2 | Bioresorbable tri-colour Si photodetector with a bioresorbable fibre optic probe for spectroscopic characterization of biological tissues. a, Schematic of a tri-colour Si photodetector, with an exploded view shown on the right. Each pair of adjacent doped layers constitutes a photojunction, with peak sensitivities at 490, 570 and 720 nm for junctions AB, BC and CD, respectively. **b**, Perspective image of the device characterized by an optical profilometer. The labels A, B, C and D indicate contact openings corresponding to layers A, B, C and D, respectively. The colour bar represents quantitative values of height. **c**, Optical microscope image of a bioresorbable spectrometer based on a tri-colour Si photodetector with four Zn electrodes (thickness: 3 μm; width: 200 μm) and a bioresorbable fibre (made from PLGA; diameter: 170 μm). **d**, Measured *I*–*V* characteristics of junction AB (blue line), BC (green line) and CD (red line) in a dark environment. **e**, Measured photoresponses of junctions AB (blue line), BC (green line) and CD (red line) as a function of illumination wavelength. The measured peak wavelengths for junctions AB, BC and CD were 490, 570 and 720 nm, respectively. **f**, Measured photovoltages generated from junction AB (blue line), BC (green line) and CD (red line) as a function of time under illumination with white light (broad-band wavelength) after passing through a chopper. **g**, Measured photovoltages generated from junction AB (blue line), BC (green line) and CD (red line) due to illumination with green and red light in a programmed sequential and combination timer. Arrows highlight the times for changes in illumination ((1) green light on, red light off; (2) green light on, red light on; (3) green light off, red light on; and (4) green light off, red light off. In **d**–**g**, $n = 6$ independent experiments.

in spectral information simultaneously and in real time (Fig. 2g, Supplementary Note VI and Supplementary Fig. 17). Encapsulating the device with a 200-nm-thick SiO_2 layer prepared by sputter deposition enables stable operation for 10 d (Supplementary Note VIII and Supplementary Fig. 21).

Bioresorbable optical filters use multi-stacks of alternating layers of SiO_x and SiN_y with a controlled periodicity or combination of several periodicities (Fig. 3) to modulate the transmission and reflection spectra in a desired manner[33,34]. Transferring such a stack from its growth substrate onto a 10-μm-thick PLGA film and drop casting another 10-μm-thick PLGA film on top locates the filter at the neutral mechanical plane to yield a flexible and fully bioresorbable optical element (Fig. 3a,b) with bending radii that can be as small as 300 μm. As shown in the cross-sectional SEM images (Fig. 3c (80° tilted view) and Supplementary Fig. 7a,b (90° tilted view)), the optical filters used here consist of multiple pairs (3–15 pairs for the examples shown here) of SiO_x and SiN_y films with thicknesses of 54 and 85 nm, respectively. The depth profile of the refractive index corresponding to 15 pairs of SiO_x and SiN_y films appears in Fig. 3d. The result is a band-stop filter with blocking wavelength from 450–520 nm and an optical density around 3.52, consistent with the simulation results (Fig. 3e; Supplementary Fig. 7c reveals that decreasing the number of pairs of SiO_x and SiN_y films decreases the optical density). Measurements of the angular dependence of the transmission spectrum show both a slight shift towards lower wavelength and a narrowing of the width of the stop-band with an increasing angle of incidence, consistent with simulation (Fig. 3f). Controlling the number of pairs of SiO_x and SiN_y films and the thickness of each film enables fabrication of bioresorbable optical filters with various filtering characteristics (Supplementary Fig. 16 and Supplementary Note X). Incorporating such a filter into a bioresorbable spectrometer by integration on the top surface of a photodetector via lamination at 55 °C enables, as an example, the detection of fluorescence-based calcium indicators of neural activity, including GCaMP (a type of genetically encoded fluorescence with an excitation wavelength of ~480 nm and an emission wavelength of ~510 nm) and Oregon Green 488 BAPTA-2 AM (a type of cell-permeable fluorescence with an excitation wavelength of 494 nm and an emission wavelength of 523 nm)[35].

Immersing these types of bioresorbable optical filters in PBS at 37 °C results in a gradual lowering of the optical transmission, mostly due to degradation of the PLGA encapsulation layer (Fig. 3g). Figure 3h provides thickness profiles and atomic force microscopy (AFM) images of pyramidal structures composed of such multilayers at several times after immersion in PBS (pH 7.4) at 80 °C (additional AFM images and thickness profiles at 80 °C and pH 5, achieved by adding acetic acid in PBS, appear in Supplementary Fig. 7). The observations indicate that the rate of dissolution (3 ± 1 nm d^{-1}) and total stress (85 MPa; compressive) of the multilayer structure are smaller than those of the individual material components, deposited under similar conditions, and similar to those for SiO_xN_y (Supplementary Fig. 7d–j). Specifically, the dissolution rates for SiO_x produced by low-frequency plasma-enhanced chemical vapour deposition (PECVD), SiN_y produced by high-frequency PECVD, SiN_y produced by low-frequency PECVD, and SiO_xN_y produced by high-frequency PECVD are 5 ± 3, 12 ± 2, 20 ± 5 and 3 ± 2 nm d^{-1}, respectively (Supplementary Fig. 7d–f,j), with corresponding film stresses of 399 (compressive), 123 (tensile), 748 (compressive) and 37 MPa (compressive), respectively (Supplementary Fig. 7g,h). These observations suggest a correlation between the residual stress and the rate of dissolution[36].

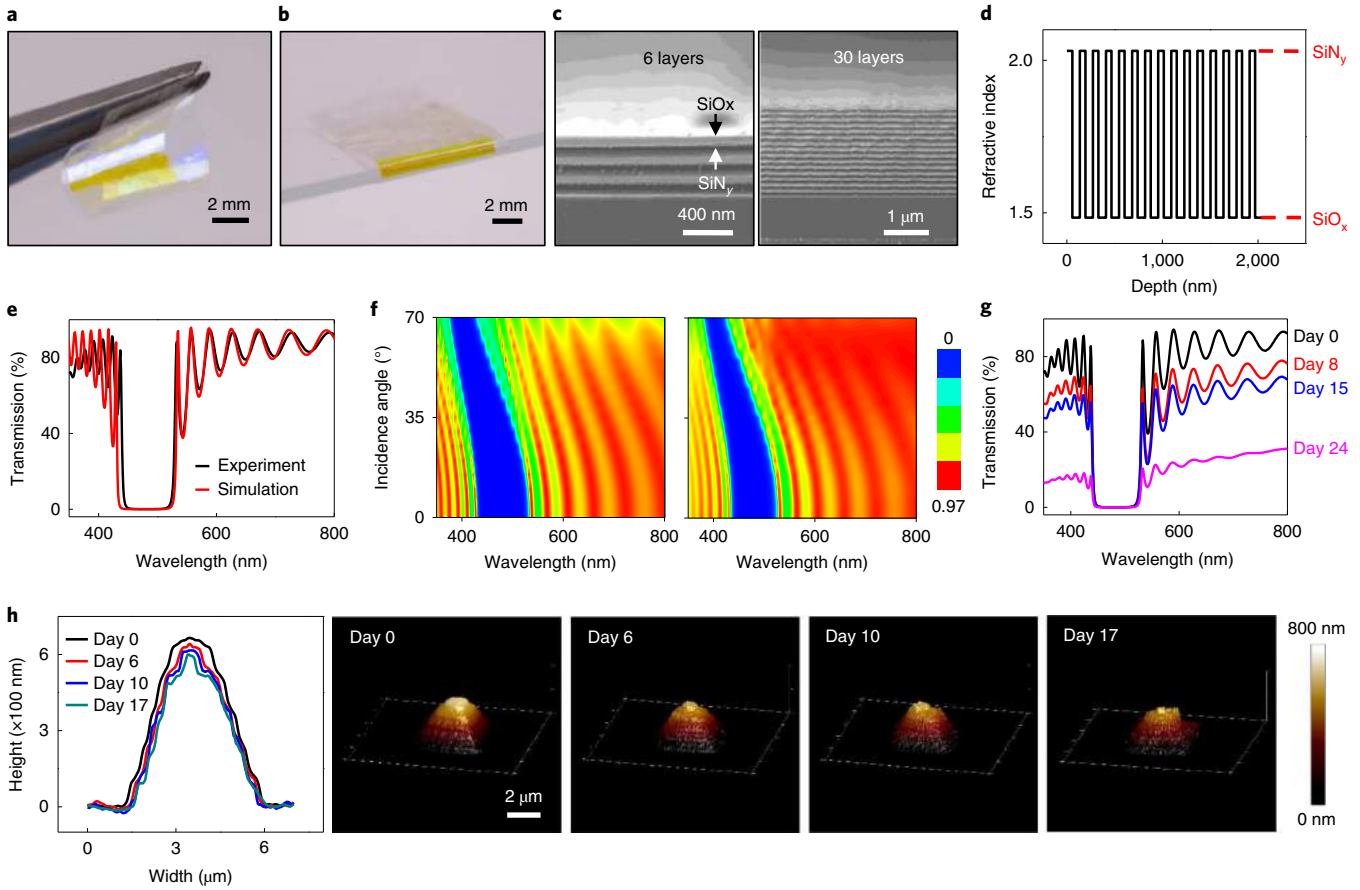

Fig. 3 | Bioresorbable optical filter based on multilayer assemblies of films of SiO_x and SiN_y. **a**, Image of a bioresorbable optical filter that consists of 15 pairs of SiO_x and SiN_y films with thicknesses of 54 and 85 nm, respectively, encapsulated by a film of PLGA with a thickness of 10 μm. **b**, Image of the filter wrapped onto the edge of a glass slide with a thickness of 1 mm. **c**, Cross-sectional SEM images (80° tilted view) of the multilayer stack. The left and right images correspond to 3 and 15 pairs, respectively, of SiO_x and SiN_y films, with total thicknesses of 417 and 2,085 nm, respectively. **d**, Depth profile of the refractive index for a filter with 15 pairs. The refractive indices of SiO_x and SiN_y are 1.48 and 2.03, respectively. **e**, Experimental and simulation results of the transmission spectrum of a filter at a 0° incidence angle. The filter effectively blocks excitation light (peak wavelength: 494 nm) and transmits emission light (peak wavelength: ~523 nm) for a Ca^{2+}-sensitive fluorophore (Oregon Green BAPTA-2 AM). **f**, Simulation (left) and experimental (right) results for transmission spectra of a bioresorbable optical filter at incidence angles between 0 and 70°. The colour bar represents quantitative values of transmission. **g**, Transmission spectra of a filter measured at various times after immersion in PBS at 37 °C. The decrease in transmission mostly arose from degradation of the PLGA substrate. **h**, Profiles (left) and AFM topographical images (right) of a multilayer of SiO_x and SiN_y patterned into a square pad with sloping sidewalls, at various times after immersion in PBS (pH = 7.4) at 80 °C. In **c**–**e**, **f** (right), **g** and **h**, $n = 3$ independent experiments.

Haematology and biochemistry studies of the biodistribution of elements (Si and Zn) associated with dissolution of the biodegradable spectrometers implanted in mouse models reveal the body's reactions to the constituent materials (surgical procedures appear in the Methods). Figure 4a,b shows concentrations of Si (Fig. 4a) and Zn (Fig. 4b) in the blood, brain, heart, kidney, liver, lung, muscle and spleen tissues explanted from mice at 1, 3, 5 and 7 weeks after implantation, measured by inductively coupled plasma optical emission spectrometry (ICP-OES) and inductively coupled plasma mass spectrometry (ICP-MS). The results in all of the measured organs of mice with an implanted device, compared with those in the control group with no implantation, showed no abnormal accumulation of dissolved Si and Zn in the tissues during the 7-week implantation period. Raised concentrations of Si and Zn appeared during the first 3 weeks of study in tissues including the blood, heart, muscle and spleen for Si, and the heart, lung and muscle for Zn, then gradually recovered to within the normal range within 7 weeks. Implantation of a Zn film (thickness 50 μm) in the subcutaneous region near the flank region showed no insoluble flakes/particles generated from the Zn film based on computed tomography (resolution: ~30 μm^3) after 41 d (Supplementary Fig. 4d). The slow increase of concentrations of Si and Zn in the kidneys (from week 1 to week 5 for Si, and from week 1 to week 7 for Zn) suggest renal clearance to maintain the metabolic balance of these materials. Histological analysis of key organ tissues (heart, kidney, lung and spleen) show no damage to the tissue and no identifiable immune cells related to implantation (Fig. 4c). Analysis of complete blood counts and blood chemistry tests also indicate no sign of organ damage or injury, and no change in the electrolyte and enzyme balance (Fig. 4d,e, Supplementary Fig. 8 and Supplementary Note II). Supplementary Fig. 9a,b shows minimal differences in changes in body weight and organ weight associated with implanted mice compared with a control group.

This type of biodegradable spectroscopic technology can be used to measure various physiological parameters that are essential in clinical care and medicine (Fig. 5 and Supplementary Fig. 26 illustrate the experimental setup). Incorporating a tunable laser (such as the NKT Photonics supercontinuum laser coupled with a SuperK VARIA tunable single-line filter) as a light source for the Si nanomembrane-based system yields transmission spectra of blood samples at various oxygenation levels that are consistent with

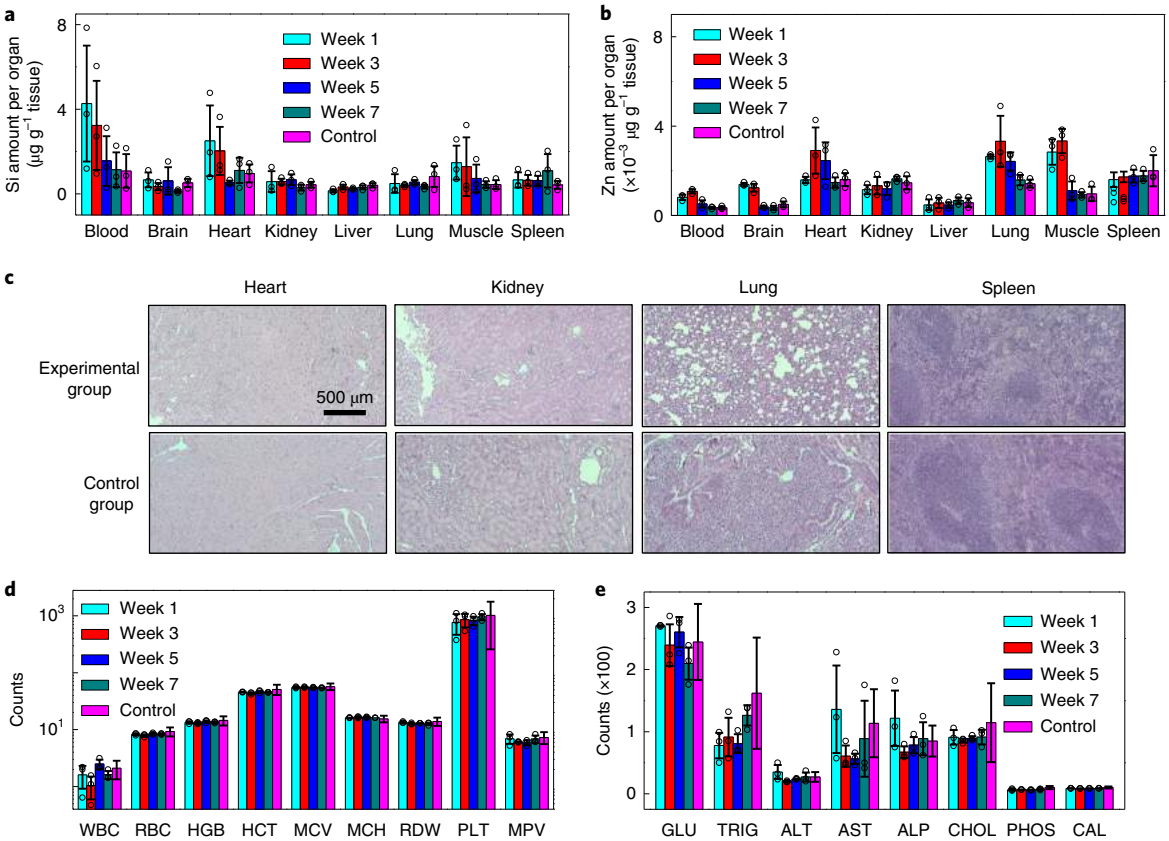

Fig. 4 | In vivo evaluations of elemental biodistribution and biocompatibility of bioresorbable devices for spectroscopic characterization of biological tissues throughout their operational period and beyond. a,**b**, In vivo biodistribution of key elements (Si (**a**) and Zn (**b**)) from bioresorbable devices for spectroscopic characterization of biological tissues. Here, the device consisted of an Si nanomembrane photodetector with the dimensions 500 μm × 500 μm × 1,500 nm (length × width × thickness), two Zn electrodes with the dimensions 2,000 μm × 250 μm × 400 nm, and a PLGA fibre with a diameter 150 μm, as shown in Fig. 1a. Implantation was in the subcutaneous region near the flank region ($n = 12$ biologically independent mice), and comparisons were made with control animals ($n = 3$ biologically independent mice). Euthanizing three experimental mice ($n = 3$ biologically independent mice) at weeks 1, 3, 5 and 7 enabled analysis of the biodistribution and biocompatibility of implanted bioresorbable spectrometers. ICP-OES and ICP-MS defined the concentrations of Si and Zn, respectively, in the blood and organs (brain, heart, kidney, liver, lung, muscle and spleen) explanted at 1, 3, 5 and 7 weeks after implantation. **c**, Histology images of the heart, kidney, lung and spleen of a control mouse and a mouse with a bioresorbable spectrometer implanted for 5 weeks ($n = 6$ independent experiments). **d**,**e**, Analysis of complete blood counts and blood chemistry for the mice in **a** and **b** ($n = 3$ biologically independent mice). Control data were provided by the mouse supplier (Charles River Laboratories). ALP, alkaline phosphatase (IU l^{-1}); ALT, alanine aminotransferase (U l^{-1}); AST, aspartate transaminase (IU l^{-1}); CAL, calcium (mg dl^{-1}); CHOL, cholesterol (mg dl^{-1}); GLU, glucose (mg dl^{-1}); HCT, haematocrit level (%); HGB, blood haemoglobin level (g dl^{-1}); MCH, mean corpuscular haemoglobin (pg); MCV, mean corpuscular volume (fl); MPV, mean platelet volume (fl); PHOS, phosphorus (mg dl^{-1}); PLT, platelet count in blood (×1,000 μl^{-1}); RBC, red blood cell (×1,000,000 μl^{-1}); RDW, red cell distribution width (%); TRIG, triglycerides (mg dl^{-1}); WBC, white blood cell (×1,000 μl^{-1}). In **a**, **b**, **d** and **e**, the results are shown as means ± s.e.m.

expectations (Fig. 5a)[37], with a linear relationship between photocurrent and oxygen saturation across the entire wavelength range (Fig. 5b). Similar strategies can be used to detect other biochemical species, including serum albumin (a common protein in the blood that is essential for stabilizing the extracellular fluid volume; Supplementary Fig. 10) and melanin (a group of natural pigments found in the body that play a critical role in epidemic health, apoptosis and some types of neural disorder; Supplementary Fig. 11 and Fig. 5c,d). Most biomedical applications rely on spectral signatures of associated chemical biomarkers[38–40]. The tri-colour Si photodetector can perform simultaneous detection at three different wavelengths (around 490, 570 and 720 nm; Fig. 5c) when operated with broad-band illumination, thus providing a basic type of continuous spectroscopy (Fig. 5d). Furthermore, the temperature-dependent resistance of the Si nanomembrane photodetector allows for monitoring of tissue temperature at a resolution of ~0.1 °C (Fig. 5e). The addition of a bioresorbable optical filter on the surface of an Si nanomembrane photodetector yields a spectrally selective response that can be aligned, for example, to the fluorescence associated with Ca^{2+} indicators for monitoring neural activity (Fig. 5f and Supplementary Fig. 12)[35]. In vitro tests show a linear relationship (Fig. 5g) between detected signals and Ca^{2+} concentration that is of biological relevance to monitoring neural activity (Fig. 5h).

Deploying these bioresorbable spectrometers in live animal models (Fig. 6 and Supplementary Fig. 14 and 15) shows possibilities for sensing cerebral temperature (Fig. 6e), cerebral oxygen saturation (Fig. 6f,g and Supplementary Fig. 14) and neural activity (Fig. 6h and Supplementary Fig. 15) continuously as the animals move in a cage environment (Fig. 6c). As shown in Fig. 7, implantation of the probes induces minimal inflammatory glial responses (day 1), which then gradually decrease over time to a level comparable to the control group, suggesting normal recovery of the mice from implantation surgery. The viability of the surrounding neurons and glia remained unchanged, compared with that of the control group. The cross-sectional area of the implantation site shows consistent decrease overtime, indicating bioresorption of implanted devices

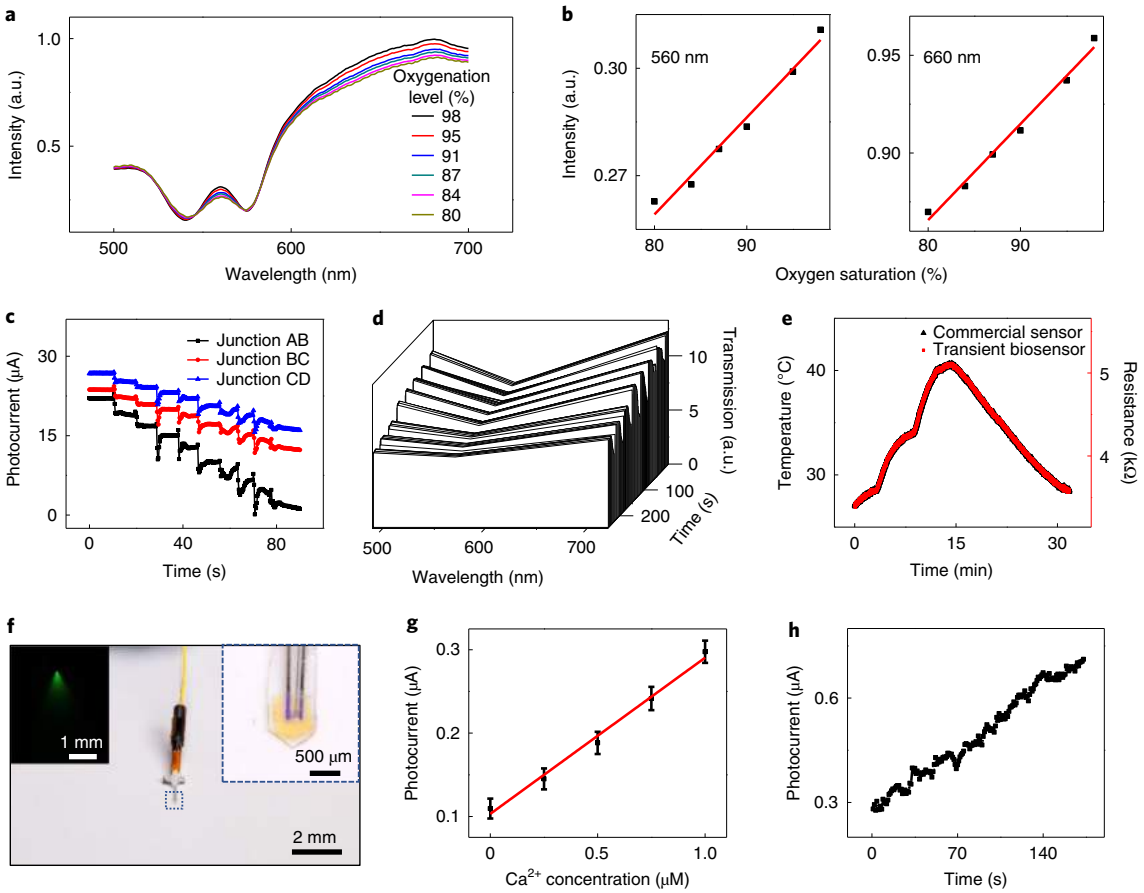

Fig. 5 | In vitro demonstrations of oxygenation, temperature, melanin and Ca^{2+} sensing via spectroscopic measurements using bioresorbable devices. **a**, Spectral response of an Si nanomembrane-based bioresorbable spectrometer to blood with various oxygenation levels. A tuneable laser delivers—through a PLGA fibre into human blood—monochromatic light with wavelengths between 450 and 750 nm. A Si nanomembrane photodetector located at the tip of the fibre generates a photoresponse at each wavelength. **b**, Calibration curves corresponding to responses at wavelengths of 560 nm (left) and 660 nm (right), measured in vitro. **c**, When exposing a bioresorbable tri-colour spectrometer to aqueous surroundings, the measured photocurrent for each junction depends on the optical properties (absorption and/or scattering) of the adjacent materials. The graph shows photocurrents measured from junctions AB, BC and CD from a bioresorbable tri-colour spectrometer during immersion in a PBS solution of melanin with concentrations varying from 0–0.1%. These concentrations are relevant to the typical melanin concentrations of human tissue. **d**, Transmission spectrum based on measurements of the bioresorbable tri-colour spectrometer, in response to melanin solutions of various concentrations from 0% (at $t = 0$ s) to 0.1% (at $t = 248$ s). **e**, Calibrated response of a bioresorbable device (red line), configured as a thermal sensor, compared with a commercial temperature sensor (black line). **f**, Image of a bioresorbable spectrometer that incorporates a bioresorbable optical filter for fluorescence sensing. Left inset: profile of emission light (wavelength: 515 nm) recorded during immersion of the bioresorbable spectrometer in Calcein solution. Excitation light (wavelength: 475 nm) is delivered through the bioresorbable polymer fibre. Right inset: enlarged view of the sensing region of the bioresorbable spectrometer with an integrated filter. The filter bonds on top of the Si nanomembrane photodetector. **g**. In vitro measurements of the bioresorbable spectrometer at various concentrations of calcium (Ca^{2+}) added into Calcein solution. The concentration of Calcein was 5 μM (pH = 13). **h**, In vitro measurements of the bioresorbable spectrometer as calcium solution constantly flowed into the Calcein solution. The concentration of Calcein was 25 μM. The flow rate of Ca^{2+} was 0.25 μM s^{-1}. In **a**–**f** and **h**, $n = 3$ independent experiments. In **g**, $n = 6$ independent experiments. The results are shown as means ± s.e.m.

with no sign of adverse effect on the neighbouring neurons. The morphologies of soma, dendrites and axons of the experimental group (days 1, 7, 14) remain similar to those of the control group (Supplementary Fig. 19), indicating minimal physiological effects on the surrounding neural and glial networks resulting from bioresorbable optical probes. Cerebral temperature reflects metabolic activity and can serve as an indicator of many diseases, such as ischaemic stroke, traumatic brain injury and subarachnoid haemorrhage[41,42]. Fig. 6e highlights such measurements performed on a mouse in the process of taking food after fasting for 5 h. The data indicate a slow increase in temperature starting at ~34.4 °C and eventually reaching ~36.8 °C, with a trajectory consistent with measurements of the skin surface using a thermal camera (Fig. 6e). The overall offset of these two measurements (~0.3 °C on average) is consistent with the expectation that the cerebral temperature should be slightly higher than the epidermal tissue. Thermal images (Fig. 6e (at time (t) = 0, 1.8 and 6.6 min)) collected at various stages of food intake also reveal an increase in body temperature, consistent with the temperature trajectory measured by the implanted device.

Cerebral oxygenation is a diagnostic indicator for various neurological diseases, including hepatic metabolic encephalopathy, meningoencephalitis and intracranial haemorrhage[43–47]. Implanting a bioresorbable spectrometer based on a tri-colour photodetector into the cerebral region near the parietal lobe (Fig. 6d and Supplementary Figs. 13 and 14) and illuminating the system with broad-band light (ranging from 450–750 nm) through the PLGA fibre enables continuous measurements of cerebral oxygenation of freely moving mice. Figure 6f shows measured photocurrents from

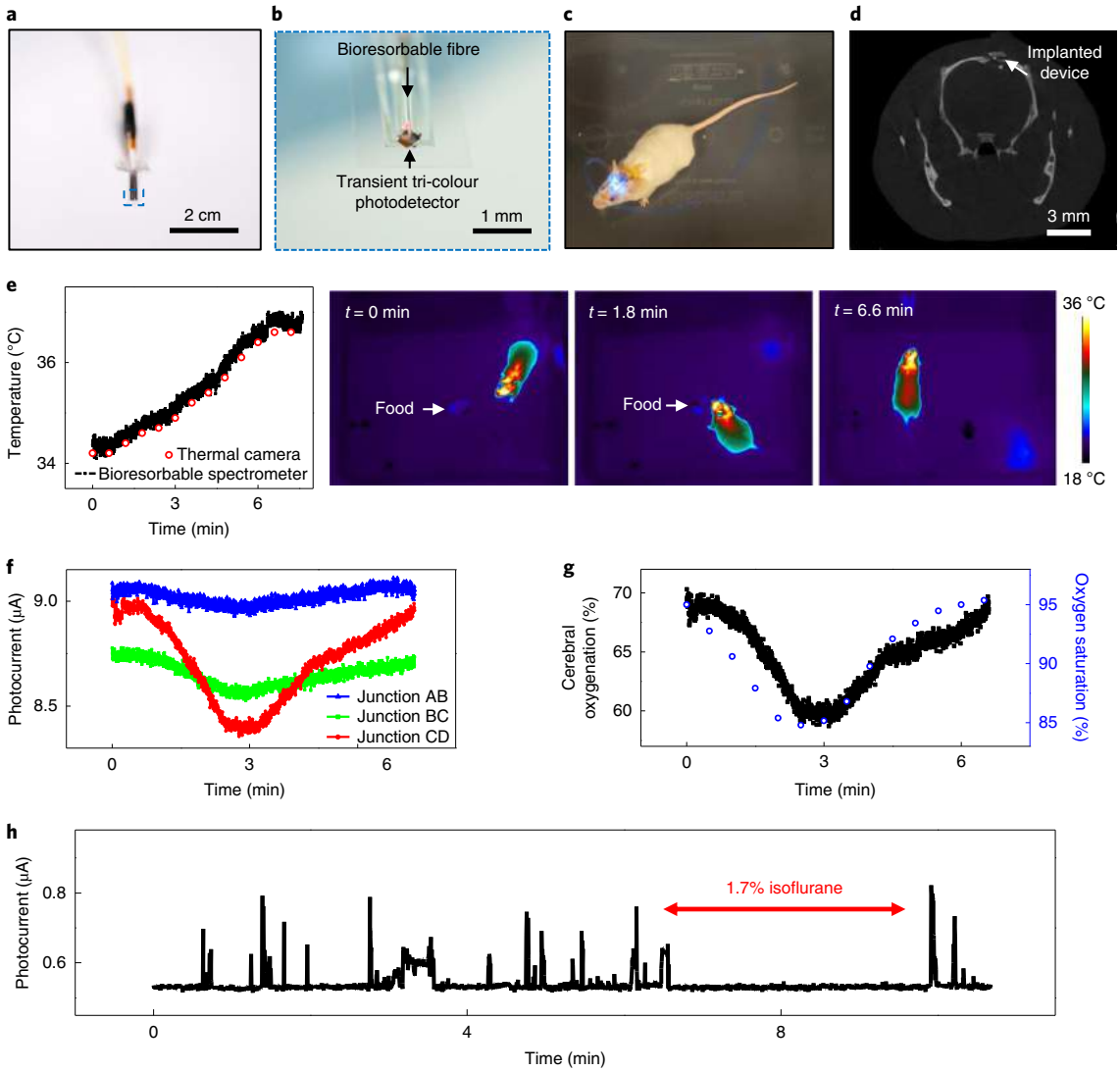

Fig. 6 | Monitoring cerebral temperature, oxygenation and neural activity in freely moving animal models via spectroscopic measurements using bioresorbable devices. a, Image of a bioresorbable spectrometer for surgical implantation into the brain. This device uses a tri-colour Si photodetector. **b**, Enlarged view of the active sensing area of the bioresorbable spectrometer. **c**, Image of a freely moving mouse implanted with a bioresorbable spectrometer. **d**, Axial-view image captured by computed tomography of a mouse implanted with a bioresorbable spectrometer. **e**, Temperature of the brain measured with an implanted bioresorbable spectrometer, and of the surface of the head of the animal using an infrared camera during tests of food intake. The corresponding thermal images (at $t = 0$, 1.8 and 6.6 min) indicate thermal distributions (in the brain and whole body) before, during and after the intake of food. **f**, Measured photocurrents from junctions AB, BC and CD of a tri-colour photodetector-based bioresorbable spectrometer implanted into the cerebral region near the parietal lobe. The environmental oxygen concentration changed from ~20% to ~7% during first 3 min of measurement, and from ~7% back to ~20% during the rest of the measurement. **g**, Cerebral oxygenation calculated based on the measurements of an implanted bioresorbable spectrometer, and blood oxygenation measured by a commercial sensor placed at the hind paw of the mice. **h**, Measured photocurrents from an implanted spectrometer in response to fluorescence (Oregon Green 488 BAPTA-2 AM) modulated by neural calcium transients, illustrating the effects of anaesthetic induction (via 1.7% isoflurane) on neuronal signalling. In **c**–**f** and h, $n = 4$ independent experiments.

junctions AB, BC and CD during changes in the environmental oxygen concentration, indicating that lowering the concentration (from ~20% to ~7%) results in a corresponding increase in light absorption from the brain tissue at wavelengths of ~490, ~570 and ~720 nm, due to the increasing percentage of deoxyhaemoglobin, consistent with a decrease in cerebral oxygenation. Based on the Beer–Lambert law, comparing light absorption measured from junctions BC and CD yields an estimate of cerebral oxygenation (Fig. 6g), consistent with measurements using a commercial oxygenation sensor (PhysioSuite for Mice & Rats; Kent Scientific) placed at the hind paw of the mice. The changes exhibit an expected time lag relative to the changes in environmental oxygen concentration.

As a third example, continuous monitoring of calcium transients in neural tissues can yield essential insights into neural function and, therefore, into the causes of and treatments for mental disorders, including clinical depression, dementia, schizophrenia and autism[48,49]. A bioresorbable optical filter (such as that shown in Fig. 3a) integrated onto an Si nanomembrane-based bioresorbable photodetector (such as that shown in Fig. 1a) implanted into an animal model with a calcium-sensitive fluorescent dye (injected before implantation of the device; amount of injection: 2 μl) allows for measurements (Fig. 6h and Supplementary Fig. 15) that reflect neural activity. Figure 6h shows the photocurrent from a device implanted into the parietal lobe of a mouse, stained with small-molecule calcium fluorescent dyes

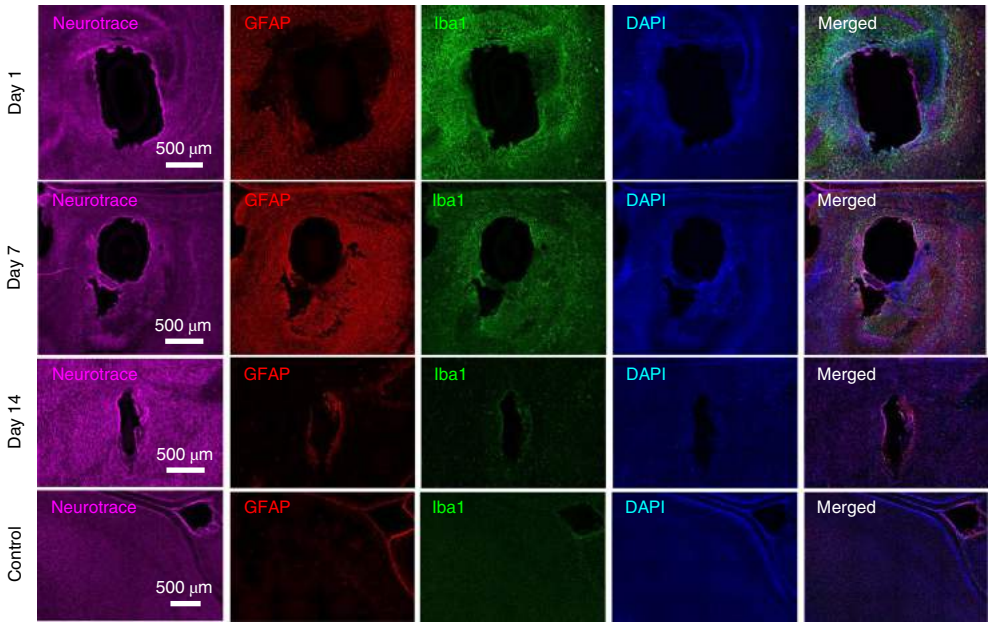

Fig. 7 | Representative confocal images of 30-μm horizontal striatal slices at various stages after implantation of the bioresorbable optical probes, compared with a control group. Probes were collected on days 1, 7 and 14, covering the typical lifetime of a bioresorbable device. The images show cross-sectional views of the implantation site with immunohistochemical staining for Nissl bodies (neurotrace, purple), astrocytes (glial fibrillary acidic protein (GFAP), red), activated microglia (Iba1, green) and DNA (4′,6-diamidino-2-phenylindole (DAPI), blue), and overall lesions from bioresorbable optical probes ($n = 3$ independent experiments).

(Oregon Green 488 BAPTA-2 AM). Anaesthesia using 1.7% isoflurane suppresses calcium transients, thereby resulting in the disappearance of spike events from in vivo measurements, consistent with existing literature, and confirming the expected operation of the device[50].

The three types of simple, bioresorbable photonic devices introduced here serve as enabling technologies for in vivo spectroscopic sensing. The components include Si nanomembrane photodetectors with wavelength-tunable light sources or with narrow-band optical filters, and tri-colour Si photodetectors with broad-band light. The small sizes of these systems minimize tissue disruption during implantation, and the biodegradability of the constituent materials leads to complete device clearance after a well-controlled operational time. Animal studies of the biodistribution of Si and Zn, the blood chemistry, and the haematology during and after the processes of bioresorption reveal no measurable toxic effects or immune responses. In vivo monitoring of cerebral temperature, cerebral oxygenation and neural activity in freely moving mice highlights some of the potential capabilities. These concepts establish unique approaches in biodegradable, or transient, photonic technologies with relevance to fundamental studies of disease pathology (such as cancer metastasis and neurological disorders) and neuroscience research, with additional possible utility in guiding surgical procedures and monitoring recovery from certain types of illness or injury.

Methods

Fabrication of the Si nanomembrane photodetector. Fabrication began with deposition of a 900-nm-thick layer of SiO_2 onto a silicon-on-insulator (SOI) substrate (thickness of Si device layer: 1,500 nm; Soitec) using PECVD. Photolithography and wet etching with buffered oxide etchant defined comb-like open areas for doping with boron (BN-1250; Saint-Gobain) at 1,000 °C for 30 min. The SiO_2 was completely removed by immersion in hydrofluoric acid solution (aqueous 49%) for 1 min. We followed similar procedures for phosphorus doping (PH-1000N; Saint-Gobain) as for boron doping (1,000 °C for 30 min). Unit cells of Si nanomembrane photodetectors were created by photolithography and reactive ion etching (SF_6 flow: 45 sccm; O_2 flow: 5 sccm; pressure: 30 mTorr; power: 150 W; 2.5 min). Immersion in hydrofluoric acid solution for 4 h fully undercut the buried oxide layer. A PDMS stamp allowed retrieval and delivery of these structures to a 10-μm-thick PLGA substrate at 60 °C on a hotplate, to complete the fabrication of the bioresorbable Si nanomembrane photodetectors. The PLGA substrate resulted from drop casting an ethyl acetate solution (7 wt%) on an Si substrate with a self-assembled monolayer formed using trimethoxymethylsilane.

Fabrication of the tri-colour photodetector. Fully formed Si NPNP junction layers fabricated on silicon-on-insulator wafers (thicknesses of NPNP junction layers: 200, 400, 1,400 and 4,500 nm, respectively; doping concentration: 10^{18} cm^{-3}; thickness of buried oxide layer: 3 μm) served as the source of bioresorbable active devices. Three consecutive processes of photolithography and reactive ion etching (SF_6 flow: 45 sccm; O_2 flow: 5 sccm; pressure: 30 mTorr; power: 150 W) opened contact areas for each junction layer. Another round of photolithography and reactive ion etching yielded isolated device unit cells. Immersion in hydrofluoric acid solution for 10 h fully undercut the buried oxide layer, thereby allowing the use of a PDMS stamp to retrieve and deliver the structures to a 10-μm-thick PLGA substrate at 60 °C on a hotplate to complete the fabrication.

Fabrication of the bioresorbable optical fibre. Fabrication began with melting PLGA (lactide:glycolide: 75:25; molecular weight: 66,000–107,000) in a small glass reservoir at 200 °C on a hotplate. Inserting a syringe needle with a diameter of 300 μm and slowly pulling it vertically yielded a PLGA fibre with a diameter of ~150 μm drawn from the reservoir. Dipping into sodium alginate solution (2 wt%) followed by immersion into a calcium chloride solution (0.5 wt%) formed a uniform cladding of bioresorbable hydrogel.

Fabrication of the bioresorbable optical filter. Alternating layers of SiO_x and SiN_y were deposited onto 100-μm-thick Si substrates using PECVD. PLGA drop cast from ethyl acetate solution (7 wt%) and baked at 70 °C, yielded a 10-μm-thick PLGA film attached to the multilayer. Etching under a vapour of xenon difluoride removed the Si handle substrate from the backside, thereby completing the fabrication.

Fabrication of the bioresorbable spectrometers. Fabrication began with lamination of a shadow mask made by laser milling on top of a bioresorbable photodetector (Si nanomembrane or tri-colour photodetector), followed by deposition of a 400-nm-thick film of Zn by electron beam evaporation to form Zn electrodes. The devices were completed by removing the shadow mask, sputtering a 50-nm-thick film of SiO_2, and aligning and attaching a bioresorbable optical filter on top at 65 °C on a hotplate.

Implantation of the bioresorbable spectrometer into the brains of live animals. All procedures associated with the animal studies followed the recommendations in the Guide for the Care and Use of Laboratory Animals of the National Institutes

of Health. The Institutional Animal Care and Use Committee at Northwestern University approved the protocol (protocol IS00005877). Female mice (CD-1; age at the initiation of the treatment: at least 6 weeks, but not more than 15 weeks; purchased from Charles River Laboratories) were acclimatized up to 5 d before surgery. Animals were anaesthetized using isoflurane gas (1–2%) during the implantation surgery. Craniotomy near the parietal lobe to the mice allowed the implantation of a bioresorbable spectrometer inside the cerebral region (Supplementary Fig. 13a). To monitor neural activity, injection of 2 µl Oregon Green (488 BAPTA-2 AM) in the parietal lobe was performed before implantation of the device. Applying dental cement (Fusio Liquid Dentin) and curing under ultraviolet light secured the implants. Mice were allowed to recover for 30 min before measurements.

Evaluation of the biodistribution, haematology and blood chemistry of mice. Overnight exposure to ultraviolet radiation sterilized the bioresorbable spectrometers, each of which consisted of an Si nanomembrane photodetector (length × width × thickness: 500 µm × 500 µm × 1,500 nm), two Zn electrodes (length × width × thickness: 10,000 µm × 200 µm × 400 nm) and a PLGA fibre (diameter: ~150 µm; length: 10,000 µm), before the implantation. The procedures involved anaesthetizing a female CD-1 mouse (Charles River Laboratories) with isoflurane gas (~2%), opening a 1-cm-length pocket at the subcutaneous region near the right flank, inserting the device into the pocket, and suturing to close the surgical opening. The procedures have been approved by the Institutional Animal Care and Use Committee of Northwestern University (protocol IS00005877). Daily checking, weighing and care of the mice ensured their moribund conditions and normal stress exposure. Euthanization of three mice at weeks 1, 3, 5 and 7 after device implantation enabled the extraction of blood, and explantation and weighing of organs, including the brain, heart, kidney, liver, lung, muscle and spleen. Charles River Laboratories conducted complete blood counts and blood chemistry tests on the blood samples collected in K-EDTA tubes and gel tubes, respectively. The explanted organs were split in half and stored in either pre-weighed 15-ml conical metal-free tubes in a −20 °C fridge or in 10% buffered formalin in 50-ml conical tubes, to prepare the tissue samples for biodistribution and histology studies, respectively. Tissues were dissolved by adding 1.5 ml nitric acid and 0.35 ml hydrogen peroxide to each tube. The tubes were kept in a water bath at 65 °C for 5 h. The dissolved tissue solutions were diluted 1:10 by adding Milli-Q water (MilliporeSigma), and analysed by ICP-OES and ICP-MS, yielding the concentrations of Si and Zn, respectively, in the tissues 1, 3, 5 and 7 weeks after implantation, to determine the biodistribution and biodegradability of dissolved Si and Zn.

Immunohistochemical analysis. Mice were given a lethal dose of pentobarbital sodium, followed by intracardial perfusion with 4% paraformaldehyde in PBS, as reported previously[51,52]. Then, the brains were dissected, post-fixed for 24 h at 4 °C, and cryoprotected with a solution of 30% sucrose in 0.1 M phosphate buffer (pH 7.4) at 4 °C for at least 24 h. This was followed by cutting into 30-µm sections, washing two or three times in PBS, and blocking in blocking buffer (PBS containing 0.5% Triton X-100 and 5% normal goat serum) for 1 h. Brain sections were then incubated for ~16 h at 4 °C in blocking buffer containing guinea pig anti-GFAP (1:500) and rabbit anti-Iba1 (1:300). After the incubation, sections were washed three times in PBS and then incubated for 2 h at room temperature in blocking buffer containing Alexa Fluor 488 goat anti-rabbit IgG (1:1,000), Alexa Fluor 568 goat anti-guinea pig IgG (1:1,000) and Neurotrace 435/455 Blue Fluorescent Nissl stain (1:100). Following the secondary antibody, sections were washed three times in PBS followed by three washes in phosphate buffer, and then mounted on glass slides with hardset Vectashield (Vector Laboratories). A Leica SP8 confocal microscope enabled imaging of all of the sections, with gain, exposure time and z-stack size remaining constant throughout each experiment. All images were processed with the same settings using the Fiji software by ImageJ.

Reporting Summary. Further information on research design is available in the Nature Research Reporting Summary linked to this article.

Data availability

The main data supporting the results of this study are available within the paper and its Supplementary Information files. The raw and analysed datasets generated during the study are available for research purposes from the corresponding author on reasonable request.

Received: 3 October 2018; Accepted: 3 July 2019;
Published online: 7 August 2019

References

1. Hotamisligil, G. S. Inflammation and metabolic disorders. *Nature* **444**, 860–867 (2006).
2. Lo, E. H., Dalkara, T. & Moskowitz, M. A. Mechanisms, challenges and opportunities in stroke. *Nat. Rev. Neurosci.* **4**, 399–414 (2003).
3. DeBerardinis, R. J. & Chandel, N. S. Fundamentals of cancer metabolism. *Sci. Adv.* **2**, e1600200 (2016).
4. Tai, L.-C. et al. Methylxanthine drug monitoring with wearable sweat sensors. *Adv. Mater.* **30**, 1707442 (2018).
5. Kim, H. et al. Single-neuronal cell culture and monitoring platform using a fully transparent microfluidic DEP device. *Sci. Rep.* **8**, 13194 (2018).
6. Bettinger, C. J. Recent advances in materials and flexible electronics for peripheral nerve interfaces. *Bioelectron. Med.* **4**, 6 (2018).
7. Hamaoka, T., McCully, K. K., Niwayama, M. & Chance, B. The use of muscle near-infrared spectroscopy in sport, health and medical sciences: recent developments. *Phil. Trans. R. Soc. A Math. Phys. Eng. Sci.* **369**, 4591–4604 (2011).
8. Ferrari, M. & Quaresima, V. A brief review on the history of human functional near-infrared spectroscopy (fNIRS) development and fields of application. *Neuroimage* **63**, 921–935 (2012).
9. Lloyd-Fox, S., Blasi, A. & Elwell, C. E. Illuminating the developing brain: the past, present and future of functional near infrared spectroscopy. *Neurosci. Biobehav. Rev.* **34**, 269–284 (2010).
10. Hwang, S.-W. et al. A physically transient form of silicon electronics. *Science* **337**, 1640–1644 (2012).
11. Kang, S. et al. Bioresorbable silicon electronic sensors for the brain. *Nature* **530**, 71–76 (2016).
12. Tao, H. et al. Silk-based resorbable electronic devices for remotely controlled therapy and in vivo infection abatement. *Proc. Natl Acad. Sci. USA* **111**, 17385–17389 (2014).
13. Luo, M., Martinez, A. W., Song, C., Herrault, F. & Allen, M. G. A microfabricated wireless RF pressure sensor made completely of biodegradable materials. *J. Micro. Syst.* **23**, 4–13 (2014).
14. Lu, L. et al. Biodegradable monocrystalline silicon photovoltaic microcells as power supplies for transient biomedical implants. *Adv. Energy Mater.* **8**, 1703035 (2018).
15. Bai, W. et al. Flexible transient optical waveguides and surface-wave biosensors constructed from monocrystalline silicon. *Adv. Mater.* **30**, 1801584 (2018).
16. Nizamoglu, S. et al. Bioabsorbable polymer optical waveguides for deep-tissue photomedicine. *Nat. Commun.* **7**, 10374 (2016).
17. Yu, K. J. et al. Bioresorbable silicon electronics for transient spatiotemporal mapping of electrical activity from the cerebral cortex. *Nat. Mater.* **15**, 782–791 (2016).
18. Fang, H. et al. Capacitively coupled arrays of multiplexed flexible silicon transistors for long-term cardiac electrophysiology. *Nat. Biomed. Eng.* **1**, 0038 (2017).
19. Son, D. et al. Bioresorbable electronic stent integrated with therapeutic nanoparticles for endovascular diseases. *ACS Nano* **9**, 5937–5946 (2015).
20. Karliczek, A. et al. Intraoperative assessment of microperfusion with visible light spectroscopy for prediction of anastomotic leakage in colorectal anastomoses. *Color. Dis.* **12**, 1018–1025 (2010).
21. Bogomolov, A. et al. Development and testing of an LED-based near-infrared sensor for human kidney tumor diagnostics. *Sensors* **17**, 1914 (2017).
22. Yun, S. H. & Kwok, S. J. J. Light in diagnosis, therapy and surgery. *Nat. Biomed. Eng.* **1**, 0008 (2017).
23. Du, Q. et al. Chip-scale broadband spectroscopic chemical sensing using an integrated supercontinuum source in a chalcogenide glass waveguide. *Photonics Res.* **6**, 506–510 (2018).
24. Warden, M. R., Cardin, J. A. & Deisseroth, K. Optical neural interfaces. *Annu. Rev. Biomed. Eng.* **16**, 103–129 (2014).
25. Kang, S.-K. et al. Dissolution behaviors and applications of silicon oxides and nitrides in transient electronics. *Adv. Funct. Mater.* **24**, 4427–4434 (2014).
26. Fu, R. et al. Implantable and biodegradable poly(L-lactic acid) fibers for optical neural interfaces. *Adv. Opt. Mater.* **6**, 1700941 (2018).
27. Lee, Y. K. et al. Dissolution of monocrystalline silicon nanomembranes and their use as encapsulation layers and electrical interfaces in water-soluble electronics. *ACS Nano* **11**, 12562–12572 (2017).
28. Yin, L. et al. Dissolvable metals for transient electronics. *Adv. Funct. Mater.* **24**, 645–658 (2014).
29. Yin, L. et al. Mechanisms for hydrolysis of silicon nanomembranes as used in bioresorbable electronics. *Adv. Mater.* **27**, 1857–1864 (2015).
30. Kang, S. K. et al. Dissolution chemistry and biocompatibility of silicon- and germanium-based semiconductors for transient electronics. *ACS Appl. Mater. Interfaces* **7**, 9297–9305 (2015).
31. Brown, J. Q., Vishwanath, K., Palmer, G. M. & Ramanujam, N. Advances in quantitative UV-visible spectroscopy for clinical and pre-clinical application in cancer. *Curr. Opin. Biotechnol.* **20**, 119–131 (2009).
32. Menon, L. et al. Transferred flexible three-color silicon membrane photodetector arrays. *IEEE Photonics J.* **7**, 1–6 (2015).
33. Liu, C. et al. High performance, biocompatible dielectric thin-film optical filters integrated with flexible substrates and microscale optoelectronic devices. *Adv. Opt. Mater.* **6**, 1800146 (2018).
34. Macleod, H. A. & Hugh, A. *Thin-Film Optical Filters* (CRC Press/Taylor & Francis, 2010).

35. Chen, T.-W. et al. Ultrasensitive fluorescent proteins for imaging neuronal activity. *Nature* **499**, 295–300 (2013).
36. Besser, R. S., Louris, P. J. & Musket, R. G. Chemical etch rate of plasma-enhanced chemical vapor deposited SiO_2 films. *J. Electrochem. Soc.* **144**, 2859–2864 (1997).
37. Kraitl, J., Timm, U. & Ewald, H. Non-invasive measurement of blood and tissue parameters based on VIS-NIR spectroscopy. In *Proc. SPIE* 8591 (SPIE, 2013).
38. Lu, G. & Fei, B. Medical hyperspectral imaging: a review. *J. Biomed. Opt.* **19**, 010901 (2014).
39. Ciurczak, E. W. & Igne, B. *Pharmaceutical and Medical Applications of Near-Infrared Spectroscopy* 2nd edn (CRC Press, 2014).
40. Durduran, T., Choe, R., Baker, W. B. & Yodh, A. G. Diffuse optics for tissue monitoring and tomography. *Rep. Prog. Phys.* **73**, 076701 (2010).
41. Mrozek, S., Vardon, F. & Geeraerts, T. Brain temperature: physiology and pathophysiology after brain injury. *Anesthesiol. Res. Pract.* **2012**, 989487 (2012).
42. Wang, H. et al. Brain temperature and its fundamental properties: a review for clinical neuroscientists. *Front. Neurosci.* **8**, 307 (2014).
43. Ho, C. L., Wang, C. M., Lee, K. K., Ng, I. & Ang, B. T. Cerebral oxygenation, vascular reactivity, and neurochemistry following decompressive craniectomy for severe traumatic brain injury. *J. Neurosurg.* **108**, 943–949 (2008).
44. Leal-Noval, S. R. et al. Invasive and noninvasive assessment of cerebral oxygenation in patients with severe traumatic brain injury. *Intensive Care Med.* **36**, 1309–1317 (2010).
45. Toet, M. C., Lemmers, P. M. A., van Schelven, L. J. & van Bel, F. Cerebral oxygenation and electrical activity after birth asphyxia: their relation to outcome. *Pediatrics* **117**, 333–339 (2006).
46. Brassard, P., Ainslie, P. N. & Secher, N. H. Cerebral oxygenation in health and disease. *Front. Physiol.* **5**, 458 (2014).
47. Van Bel, F. & Mintzer, J. P. Monitoring cerebral oxygenation of the immature brain: a neuroprotective strategy? *Pediatr. Res.* **84**, 159–164 (2018).
48. Tye, K. M. & Deisseroth, K. Optogenetic investigation of neural circuits underlying brain disease in animal models. *Nat. Rev. Neurosci.* **13**, 251–266 (2012).
49. Cui, G. et al. Concurrent activation of striatal direct and indirect pathways during action initiation. *Nature* **494**, 238–242 (2013).
50. Thrane, A. S. et al. General anesthesia selectively disrupts astrocyte calcium signaling in the awake mouse cortex. *Proc. Natl Acad. Sci. USA* **109**, 18974–18979 (2012).
51. Siuda, E. R., Al-Hasani, R., McCall, J. G., Bhatti, D. L. & Bruchas, M. R. Chemogenetic and optogenetic activation of Gαs signaling in the basolateral amygdala induces acute and social anxiety-like states. *Neuropsychopharmacology* **41**, 2011–2023 (2016).
52. Jeong, J.-W. et al. Wireless optofluidic systems for programmable in vivo pharmacology and optogenetics. *Cell* **162**, 662–674 (2015).

Acknowledgements

W.Z. acknowledges support from the Army Research Office under grant W911NF-15-1-0035. This work utilized the Northwestern University Micro/Nano Fabrication Facility, which is partially supported by the Soft and Hybrid Nanotechnology Experimental Resource (NSF ECCS-1542205), Materials Research Science and Engineering Center (NSF DMR-1121262), State of Illinois, Northwestern University and Center for Bio-Integrated Electronics (Simpson Querrey Institute). The Center for Developmental Therapeutics is supported by Cancer Center Support Grant P30 CA060553 from the National Cancer Institute, awarded to the Robert H. Lurie Comprehensive Cancer Center.

Author contributions

W.B., R.F., J.S., D.L., X.N., Y.P., Z.L., T.H., Y.L., D.W., H.Z., X.S., L.Y., W.Z. and J.A.R. designed and fabricated the devices, and performed the analysis. W.B., I.K., J.S., D.L., X.N., Y.P., I.S. and F.A. performed the animal study. C.R.H. and A.B. performed the computed tomography imaging. W.B., I.K, J.S., D.W., X.N., Q.Y., J.Z., K.M. and M.P. performed the study of bioresorption, biodistribution and toxicity. W.B., J.S., I.K., R.F., W.Z. and J.A.R wrote the manuscript with input from all authors.

Competing interests

The authors declare no competing interests.

Additional information

Supplementary information is available for this paper at https://doi.org/10.1038/s41551-019-0435-y.

Reprints and permissions information is available at www.nature.com/reprints.

Correspondence and requests for materials should be addressed to J.A.R.

Publisher's note: Springer Nature remains neutral with regard to jurisdictional claims in published maps and institutional affiliations.

nature biomedical engineering

SUPPLEMENTARY INFORMATION

https://doi.org/10.1038/s41551-019-0435-y

In the format provided by the authors and unedited.

Bioresorbable photonic devices for the spectroscopic characterization of physiological status and neural activity

Wubin Bai[1,2,20], Jiho Shin[3,20], Ruxing Fu[4,20], Irawati Kandela[5,6], Di Lu[1,2], Xiaoyue Ni[1,2], Yoonseok Park[1,2], Zhonghe Liu[7], Tao Hang[8], Di Wu[2,9], Yonghao Liu[7], Chad R. Haney[6,10], Iwona Stepien[5,6], Quansan Yang[2,11], Jie Zhao[1,2], Khizar Rehan Nandoliya[12], Hao Zhang[1,2,13], Xing Sheng[14], Lan Yin[4], Keith MacRenaris[6,10], Anlil Brikha[6,10], Fraser Aird[5,6], Maryam Pezhouh[15], Jessica Hornick[16], Weidong Zhou[7] and John A. Rogers[1,2,9,11,12,17,18,19]★

[1]Department of Materials Science and Engineering, Northwestern University, Evanston, IL, USA. [2]Center for Bio-Integrated Electronics, Northwestern University, Evanston, IL, USA. [3]Department of Chemical and Biomolecular Engineering, University of Illinois Urbana–Champaign, Urbana, IL, USA. [4]School of Materials Science and Engineering, Tsinghua University, Beijing, China. [5]Center for Developmental Therapeutics, Northwestern University, Evanston, IL, USA. [6]Chemistry Life Processes Institute, Northwestern University, Evanston, IL, USA. [7]Department of Electrical Engineering, University of Texas at Arlington, Arlington, TX, USA. [8]State Key Laboratory of Metal Matrix Composites, School of Materials Science and Engineering, Shanghai Jiao Tong University, Shanghai, China. [9]Department of Biomedical Engineering, Northwestern University, Evanston, IL, USA. [10]Center For Advanced Molecular Imaging, Northwestern University, Evanston, IL, USA. [11]Department of Mechanical Engineering, Northwestern University, Evanston, IL, USA. [12]Department of Chemistry, Northwestern University, Evanston, IL, USA. [13]Department of Chemistry, Key Laboratory of Bioorganic Phosphorus Chemistry & Chemical Biology, Tsinghua University, Beijing, China. [14]Department of Electronic Engineering, Tsinghua University, Beijing, China. [15]Northwestern Medicine, Feinberg School of Medicine, Northwestern University, Evanston, IL, USA. [16]Biological Imaging Facility, Northwestern University, Evanston, IL, USA. [17]Department of Neurological Surgery, Northwestern University, Evanston, IL, USA. [18]Department of Electrical and Computer Engineering, Northwestern University, Evanston, IL, USA. [19]Simpson Querrey Institute for BioNanotechnology, Northwestern University, Evanston, IL, USA. [20]These authors contributed equally: Wubin Bai, Jiho Shin, Ruxing Fu. *e-mail: jrogers@northwestern.edu

Table of Contents

Supplementary Note I. Bioresorbable fiber

Supplementary Figures 1b&c show propagation of red light (wavelength 660 nm) through a fiber in air and embedded in chicken breast, respectively. The measured propagation loss (at wavelength 660 nm) in the latter medium for an unclad fiber is 1.6±0.2 dB/cm, which is significantly larger than that (0.6±0.2 dB/cm) measured in air (Supplementary Figure 1d), as expected. As shown in Supplementary Figure 1e, the propagation losses (at a wavelength of 660 nm) in air and chicken breast for a clad fiber are 0.8±0.1 dB/cm and 0.9±0.2 dB/cm, respectively. Supplementary Figure 1f shows that the bending losses of clad fibers in air and milk are small for radii of curvatures ranging from 4 mm to 12 mm.

Supplementary Note II. Study on biodistribution and toxicity of the bioresorbable optical probes

The 7-week period of study shows no significant change in average count of white blood cells (WBC), red blood cells (RBC), platelets (PLT), hemoglobin (HGB), hematocrit (HCT), mean corpuscular volume (MCV), mean corpuscular hemoglobin (MCH), red cell distribution width (RDW), platelet count (PLT), and mean platelet volume (MPV), indicating absence of any abnormalities, including anemia, nutritional deficiency, liver disease, bleeding disorder, and heart attack (Figure 4d. Supplementary Figure 8).

Blood chemistry tests additionally yield information on enzymes and electrolytes, as diagnostic biomarkers of organ-specific diseases and metabolic disorders. The results fall within confidence intervals of control values (Figure 4d and Supplementary Figure 8). Specifically, normal levels of albumin (ALB), total protein (TP), alanine aminotransferase (ALT), alkaline phosphatase (ALP), aspartate transaminase (AST) indicate normal liver function. Normal levels of blood urea nitrogen (BUN), creatine (CREA) indicate normal kidney function. Normal levels of glucose (GLU), calcium (Ca), sodium (Na), potassium (K), chloride (Cl), and phosphorus (PHOS) suggest normal function of the metabolic system.

Supplementary Note III. Plasmas-enhanced chemical vapor deposition for making the multilayer optical filter

Deposition parameters (including temperature, pressure, flow rate, power, and others) in plasmas-enhanced chemical vapor deposition (PECVD) can influence the properties of the resulting films, such as their index of refraction, oxide charge, surface roughness, residual stress, etch rate, film morphology, dissolution rate, and others. For example, varying flows of reactant gases: N_2O and NH_3 at a constant flow of SiH_4 in PECVD enable modulation of the refractive index of SiO_xN_y, which also shows monotonic relationships with the residual stress and atomic ratio of oxygen and nitrogen.[1–3]

Here, deposition of films of low-frequency (LF, 380 kHz) SiO_x, high-frequency (HF, 13.56 MHz) SiN_y, LF SiN_y and HF SiO_xN_y involve the following PECVD conditions, with measured residual stress and dissolution profiles shown in Supplementary Figure 7 d-j:

1) LF SiO_x: pressure 550 mTorr, N_2O flow: 1420 sccm, SiH_4 flow: 120 sccm, N_2 flow: 872 sccm, power: 60 W, 300 ^oC

2) HF SiN_y: pressure 900 mTorr, NH_3 flow: 55 sccm, SiH_4 flow: 400 sccm, N_2 flow: 3000 sccm, power: 30 W, 300 ^oC
3) LF SiN_y: pressure 550 mTorr, NH_3 flow: 20 sccm, SiH_4 flow: 400 sccm, N_2 flow: 1600 sccm, power: 60 W, 300 ^oC
4) HF SiO_xN_y: pressure 900 mTorr, NH_3 flow: 300 sccm, SiH_4 flow: 100 sccm, N_2 flow: 400 sccm, N_2O flow: 1420 sccm, power: 30 W, 300 ^oC
5) Multilayer filter of SiO_x and SiN_y:
   LF SiO_x: pressure 550 mTorr, N_2O flow: 1420 sccm, SiH_4 flow: 120 sccm, N_2 flow: 872 sccm, power: 60 W, 300 ^oC
   HF SiN_y: pressure 900 mTorr, NH_3 flow: 55 sccm, SiH_4 flow: 400 sccm, N_2 flow: 3000 sccm, power: 30 W, 300 ^oC

Supplementary Note IV. in vitro demonstrations of oxygenation sensing via spectroscopic measurements using bioresorbable devices

Figure 5a&b shows in vitro demonstrations of oxygenation sensing via spectroscopic measurements using bioresorbable devices. Here, human blood (purchased from Sigma-Aldrich) is contained in a reservoir, which is maintained at 37.0±0.1 ^oC by a temperature controller. The amount of sodium dithionite added in the blood defines the oxygenation level, across a relevant range.

Supplementary Note V. Tailoring filtering characteristics of the bioresorbable optical filters

To demonstrate the sensing capabilities at multiple wavelengths across a wavelength range of interest using SiOx-and-SiNy multilayer optical filters, we designed and fabricated six different types of filters with refractive index profiles shown in Supplementary Figure 16a, c, e, g, i, and k. Supplementary Figure 16b, d, f, h, j, and l show the corresponding transmission spectrums, respectively. Specifically, Supplementary Figure 16b, f, h, j, and l exhibit narrow-band transmission at wavelengths of 503 nm, 525 nm, 550 nm, 650 nm, and 833 nm, respectively. Supplementary Figure 16d shows a band-block filter with blocking wavelength ranging from 430 nm to 520 nm. These results illustrate the ability to use bioresorbable multilayer optical filters for sensing at a diverse range of programmed wavelengths, as essential components for applications including florescence sensing and imaging, optically controlled switches, optical stimulations, and others.

Supplementary Note VI. A Red-Green-Blue (RGB) Color Model for Tri-color Spectroscopic Sensing

A Red-Green-Blue (RGB) color model serves as a consistent approximation to resolve the wavelengths:[4,5]

$$(P_{490\,nm} \quad P_{570\,nm} \quad P_{720\,nm}) = \begin{pmatrix} a_{11} & a_{12} & a_{13} \\ a_{21} & a_{22} & a_{23} \\ a_{31} & a_{32} & a_{33} \end{pmatrix} \times \begin{pmatrix} A_{AB} \\ A_{BC} \\ A_{CD} \end{pmatrix}$$

where $A_{AB}, A_{BC}, and\ A_{CD}$ are measured photocurrents from junction AB, BC, and CD, respectively; $P_{490\,nm}, P_{570\,nm}, and\ P_{720\,nm}$ are calculated photo intensities corresponding to wavelengths 490 nm,

570 nm, and 720 nm; $a_{11}, a_{12}, \cdots, a_{33}$ correlate with spectral responsivity, and can be calibrated from responsivity measurements for each junction.

Supplementary figure 17 shows the performance of three tri-color Si photodetectors in response to modulated illumination with a square-wave profile. All devices show consistent responses to the variations in spectral characteristics of illuminated light. The measured signal-to-noise ratios are all larger than 50 dB, comparable with industrial standards.[4,5]

Supplementary Note VII. Immunohistochemical analysis on the bioresorbable optical probes

Supplementary Figure 19 shows an immunohistochemical study across the typical lifetime (~ 2 weeks) of a bioresorbable optical probes (n=3 for each time point). Implantation of the probes induces minimal inflammatory glial responses (day 1), comparable with previously reported implantation procedure, and then gradually decrease overtime to the level comparable to the control group, suggesting normal recovery of the mice from implantation surgery. The viability of the surrounding neurons and glia remained unchanged, compared with that of control group. The cross-sectional area of implantation site shows a consistent decrease overtime, indicating bioresorption of implanted devices with no sign of adverse effect to the neighboring neurons. The morphologies of soma, dendrites, and axon of experimental group (Day 1, 7, 14) remain similar to those of control group (Supplementary Figure 19), indicating minimal physiological effector on the surrounding neural and glial networks resulted from bioresorbable optical probes.

Supplementary Note VIII. Dissolution behavior of a tri-color silicon photodetector on its performance of photosensing

The measured results in Supplementary Figure 21 show that an encapsulation layer of SiO_2 (thickness 200 nm) can effectively maintain the spectroscopic sensing performance of the tri-color silicon photodetector for around 10 days, which is consistent with the reported dissolution rate of sputtered SiO_2, 8 – 15 nm/day in phosphate-buffered saline (PBS) at 37 ^{o}C.[6,7] After 10 days of immersion in PBS, the slopes of the I-V curves in the forward bias mode gradually decrease for all three junctions (AB, BC, CD) as hydrolysis reactions appear at both the sensing area and contact pads of the photodetector. On day 20 (Supplementary Figure 21), the measured responsivity and wavelength selectivity show significant decreases. On day 30, the essential I-V characteristics of photodiode become undetectable for all three junctions (AB, BC, CD).

Supplementary Note VIIII. Simulation model to analyze the light detected by the silicon photodetector of the bioresorbable optical probe

To quantitatively evaluate the optical sensing process in tissue, we establish a ray-tracing model to calculate the intensity of effective sensing light. In this model (Supplementary Figure 23), the tip of the optical fiber is placed next to the detector, following the same geometrical layout of the bioresorbable optical probe (Figure 1c). The biological tissue serves as an optical medium with highly absorbing and

scattering properties (optical absorption coefficient is ~0.2 /mm at the wavelength of 480 nm; its scattering coefficient is 47 /mm with anisotropy of 0.85 (g=0.85) at the wavelength of 480 nm).[8,9]

The fiber has the same dimensions (diameter, 200 mm; length, 5 mm in brain tissue) as those in the experiment (Figure 1) and share the same optical properties with PLGA. A simulated silicon photodetector (dimension, 0.5×0.5×0.1 mm3) is placed at the tip of the fiber and we compute the flux of incident light on the upper surface of photodetector. The detected intensity accounts 20.9 % of the total from the light source. If we remove the brain tissue and use free space as optical media, the light intensity on the upper surface of photodetector decreases to 8.9 % of the total, suggesting that the highly scattering tissue expands the optical path length such that the majority (more than 57.4%) of detected light from the photodetector passes through the interaction with the tissue.

Supplementary Note X. Simulation Model on multilayer optical sensor for fluorescent sensing

We also establish a model (with model design shown in Supplementary Figure 25) to calculate the measurements of fluorescence using the bioresorbable optical probe. Here we use Oregon-Green BAPTA-2 AM as Ca2+ indicators, with associated optical properties including emission spectrum, quantum efficiency (0.7), and peak molar extinction (135000 L/ mol·cm), collected from literature.[10] We assume the dye is filled in a sphere area with a radius of 2 mm and a concentration of 2 μM. Supplementary Figure 25c&d show simulated intensity profiles for excitation light delivered from light source and relatively static over time, and for fluorescent light emitted from Ca2+ indicators, where the intensity is proportional to the concentration of calcium ions. For a typical physiological concentration of calcium ion (~ 4 μM), the intensities of excitation light and fluorescent light at the top surface of the optical filter account 10.2 % and 0.83 % of the total from the light source, respectively. The measured optical density for the optical filter shown in Figure 3 is ~3.52 (Supplementary Figure 25b). The results show that after passing through the multilayer optical filter (Figure 3), the transmitted light includes some small contribution from excitation light (~0.05 % of the total from light source), but is mainly due to fluorescent light (~ 0.7 % of the total). As a result, the response of the photodetector with the optical filter is dominated by the fluorescent light, and represents calcium activity, which is consistent with in vitro observations (Figure 5g&h).

Supplementary Note XI. Experimental Setup for In vitro measurements

The experimental setup includes: 1) a tunable laser (NKT photonics supercontinuum laser, integrated with SuperK VARIA tunable single line filter) which generates light of a single wavelength, multiple wavelengths, or a range of wavelengths; 2) a commercial fiber which connects to the PLGA fiber and delivers light to the bioresorbable sensing probe; 3) a data acquisition system (Keysight Technologies 347970A) that connects to a computer and records electrical measurements of multiple electrical channels; 4) 4 electrode connectors that connects the electrodes of bioresorbable sensing probe with the data acquisition system; 5) a sample reservoir that contains blood sample for oxygenation measurement (Figure 5a&b) and for melanin measurement (Figure 5c&d), or Calcein solution for measurement of calcium concentration (Figure 5f-h); 6) a fluidic channel that enable a controlled flow of sodium dithionite dissolved in blood for oxygenation measurement, or melanin

dissolved in phosphate-buffered saline (PBS) for melanin measurements, or calcium chloride dissolved in phosphate-buffered saline (PBS) for measurement of calcium concentration; The temperature is maintained by a temperature controller. 7) a translation stage that stabilizes the position of the bioresorbable sensing probe inside sample reservoir. The temperature measurement follows a similar setup except that the fluidic channel is replaced with a thermocouple and a heating stage is included underneath the sample reservoir. The optical power used for the in vitro measurement is around 0.7 mW. (b) an enlarged view of sample reservoir to show the bioresorbable sensing probe and the fluid channel.

References

1. Han, J., Yin, Y. J., Han, D. & Dong, L. Z. Improved PECVD SixNyfilm as a mask layer for deep wet etching of the silicon. *Mater. Res. Express* **4,** 096301 (2017).

2. Jozwik, M., Gorecki, C., Delobelle, P., Sabac, A. & Kujawinska, M. Evaluation of the mechanical properties of square membranes prestressed by PECVD silicon oxynitride thin films. in (eds. Osten, W. & Novak, E.) **5532,** 326 (International Society for Optics and Photonics, 2004).

3. Tarraf, A., Daleiden, J., Irmer, S., Prasai, D. & Hillmer, H. Stress investigation of PECVD dielectric layers for advanced optical MEMS. *J. Micromechanics Microengineering* **14,** 317–323 (2004).

4. Cameras—Determination, P. S.-P. of ISO Speed. *ISO Stand.* **12232,** (1998).

5. Anderson, M., Motta, R., Chandrasekar, S. & Stokes, M. Proposal for a standard default color space for the internet—srgb. in *Color and imaging conference* **1996,** 238–245 (Society for Imaging Science and Technology, 1996).

6. Fang, H. *et al.* Ultrathin, transferred layers of thermally grown silicon dioxide as biofluid barriers for biointegrated flexible electronic systems. *Proc. Natl. Acad. Sci. U. S. A.* **113,** 11682–11687 (2016).

7. Kang, S. *et al.* Bioresorbable silicon electronic sensors for the brain. *Nature* **530,** 71–76 (2016).

8. Jacques, S. L. Corrigendum: Optical properties of biological tissues: a review. *Phys. Med. Biol.* **58,** 5007–5008 (2013).

9. Tuchin, V. V., Utz, S. R. & Yaroslavsky, I. V. Tissue optics, light distribution, and spectroscopy. *Opt. Eng.* **33,** 3178 (1994).

10. Paredes, R. M., Etzler, J. C., Watts, L. T., Zheng, W. & Lechleiter, J. D. Chemical calcium indicators. *Methods* **46,** 143–151 (2008).

Supplementary Table 1 | Performance of Bioresorbable Photodetector based on 1500 nm-thick monocrystalline Si nanomembrane

	Green (530 nm)	**Red (630 nm)**
Current @-1v	5 uA	1.8 uA
Power	37 uW	13.5 uW
Responsivity(A/W)	0.135	0.133
Q.E	0.315	0.26

Supplementary Table 2 | Basic Parameters of Tri-color photodetector

Layer	Doping Type	Doping Concentration (cm^{-3})	Thickness (nm)
A Layer	n+	10^{18}	200
B Layer	p+	10^{18}	400
C Layer	n+	10^{18}	1400
D Layer	p+	10^{18}	4500

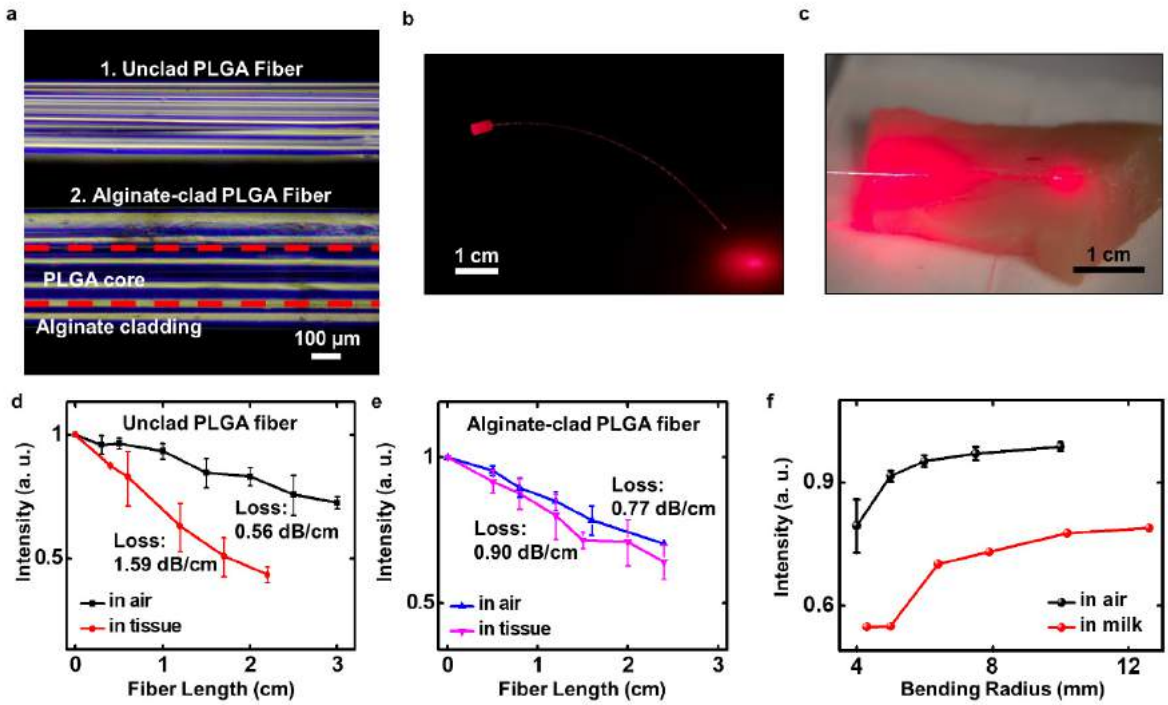

Supplementary Figure 1. Bioresorbable optical fibers and their performance.

(a) Upper image: Unclad PLGA fiber; Lower image: Alginate-clad PLGA fiber. (b) Image of light propagation through an unclad PLGA fiber suspended in air. (c) Image of light propagation through an alginate-clad PLGA fiber embedded in chicken meat. (a-c) n=6 independent experiments. (d) Measured transmission intensity of the unclad PLGA fiber in air and embedded in chicken meat, as a function of fiber length. The measured propagation losses in air and in chicken meat are 0.56 dB/cm and 1.59 dB/cm, respectively. (e) Measured transmission intensity of alginate-clad PLGA fiber in air and embedded in chicken meat, as a function of fiber length. The measured propagation losses in air and in chicken meat are 0.77 dB/cm and 0.90 dB/cm, respectively. (f) Measured transmission intensity of an alginate-clad PLGA fiber in air and milk, at various bending radii. (b)-(f) Light wavelength: 633 nm. (d-f) n=6 independent experiments. Results are shown as means ± s.e.m.

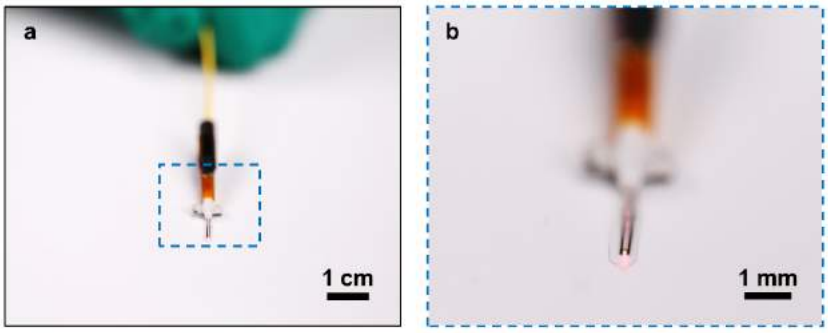

Supplementary Figure 2. Implantable bioresorbable spectrometer based on a Si NM photodetector and a bioresorbable fiber optic probe.

(a) Image of an implantable bioresorbable spectrometer based on Si NM (1500 nm in thickness) photodetector interfaced to a bioresorbable fiber optic probe. (b) Enlarged view of sensing region of the device.

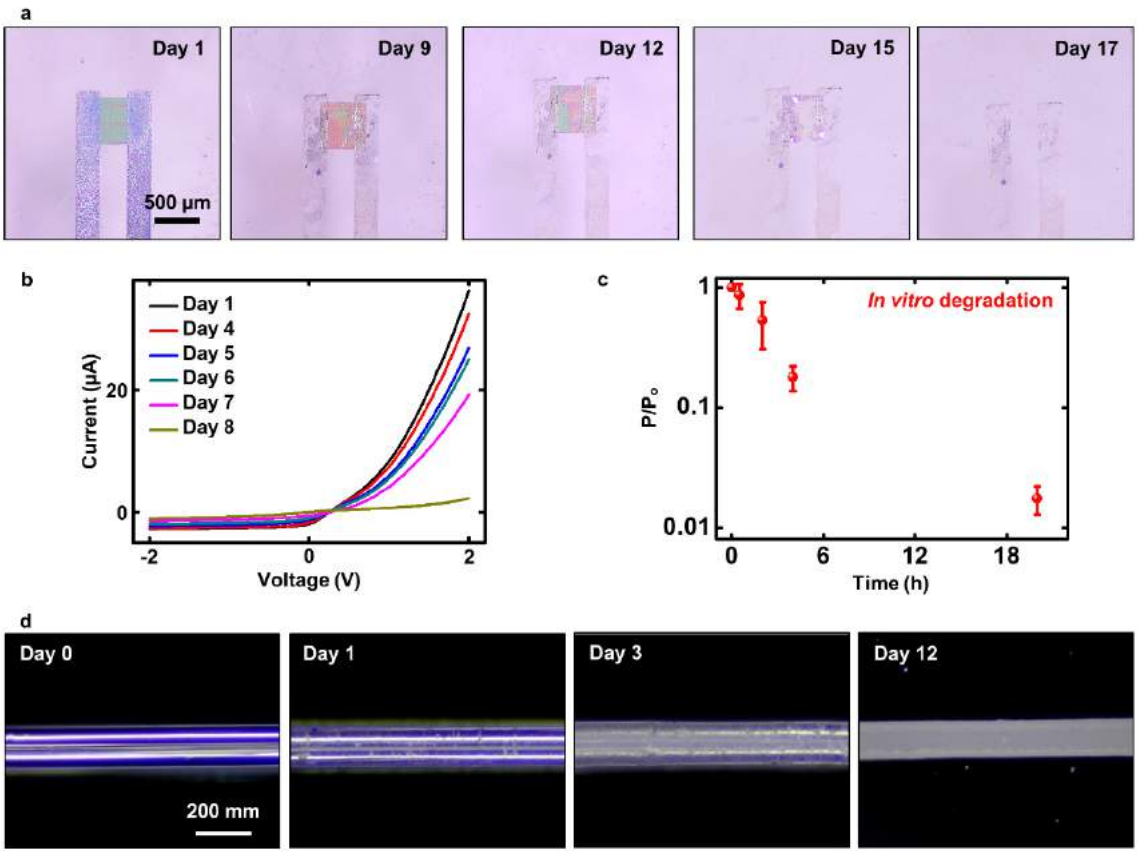

Supplementary Figure 3. Dissolution behaviors of key components (bioresorbable Si NM photodetector and PLGA fiber) of a bioresorbable device for spectroscopic characterization of biological tissues.

(a) Images of a bioresorbable Si NM photodetector at various stages of immersion in phosphate-buffered saline (PBS) at 37 ^{o}C. Thickness of Si NM: 300 nm. All images share the same scale bar. (b) Measured I-V characteristics (under illumination of broadband light ranging from 450 nm to 750 nm) of the device at various stages of immersion in phosphate-buffered saline at 37 ^{o}C. (a-b) n=6 independent experiments. (c) Measurements of optical attenuation of a PLGA fiber (diameter 150 μm) during immersion in PBS at 37 ^{o}C. P: measured output light intensity. P_o: the highest measured output light intensity at day 1. n=6 independent experiments. Results are shown as means ± s.e.m.. (d) Corresponding images of a PLGA fiber (diameter 150 μm) during immersion in PBS at 37 ^{o}C. Optical images captured on day 0, 1, 3, and 12 indicate a decrease in optical transparency. All images share the same scale bar. n=6 independent experiments.

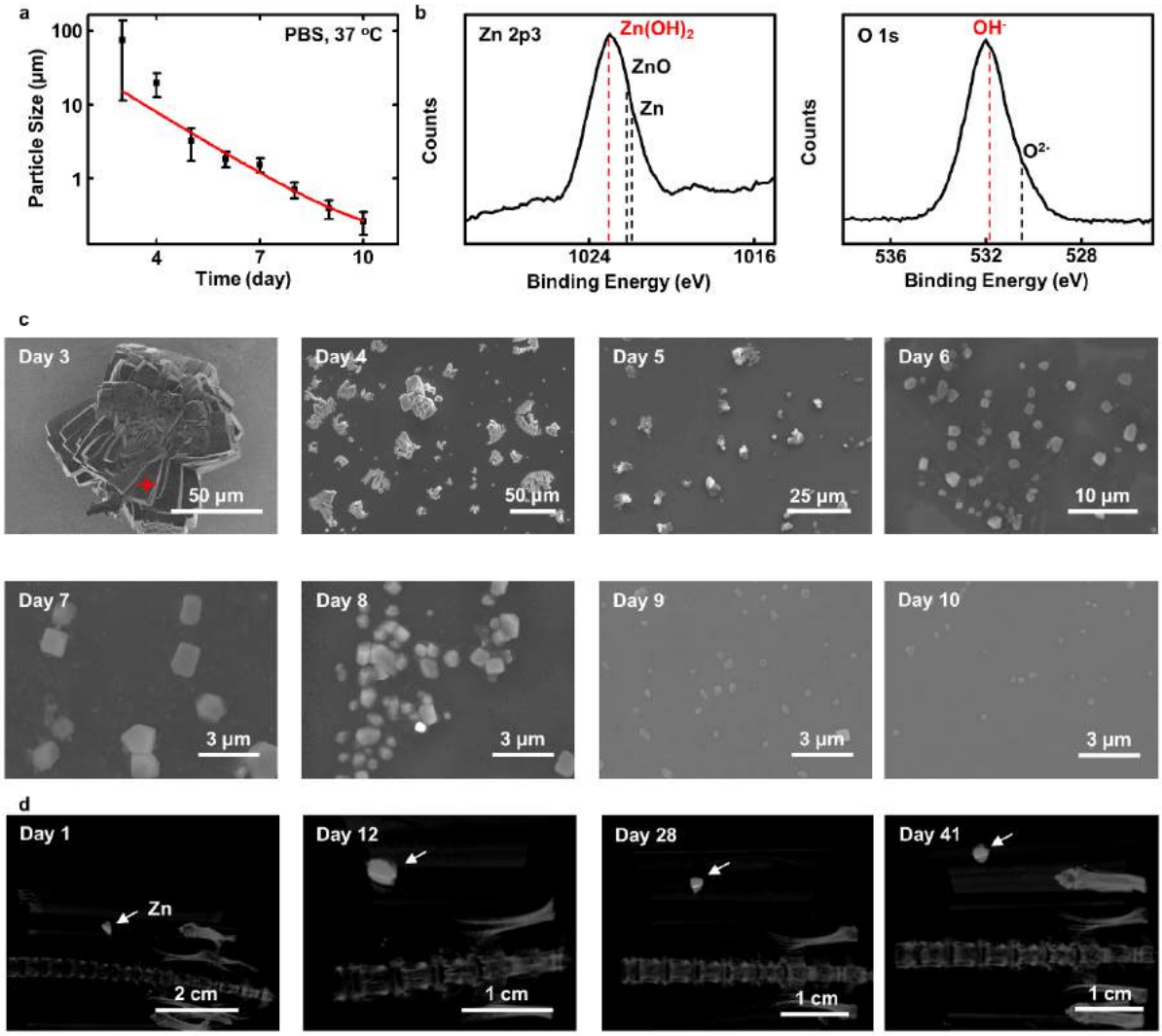

Supplementary Figure 4. Dissolution and in vivo bioresorption of Zn films.

(a) Measured size of particles and platelets generated by dissolution induced fracture of a film of Zn (thickness 1 μm) during immersion in PBS at 37 °C. The Zn film is prepared by electron beam evaporation on a Si substrate. Particle sizes are calibrated via SEM images captured on day 3, 4, 5, 7, 8, 9, and 10. n=6 independent experiments. Results are shown as means ± s.e.m.. (b) Energy-dispersive X-ray spectroscopy analysis of a fragment captured on day 7 at the location indicated by a red cross in the SEM image. (c) Representative SEM images of the fragments captured on day 3, 4, 5, 7, 8, 9, and 10. Red cross indicates the area where energy-dispersive X-ray spectroscopy was performed. (b-c) n=6 independent experiments. (d) 3D-rendered unfiltered computed tomography (CT) images of a mouse collected over 41 days after implantation of a Zn film (thickness 50 μm, width x length 2 mm x 2 mm). n=3 biologically independent animals. Arrows indicate location of the Zn film. The Zn film was implanted at subcutaneous region near the right thigh of mice. The images indicate implantation of the Zn film produces no observable fragments or particle.

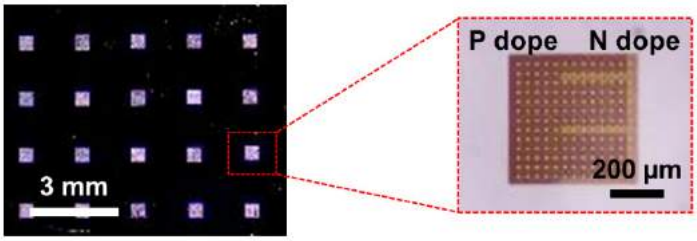

Supplementary Figure 5. Image of arrays of bioresorbable Si NM photodetectors used for in vivo tests of bioresorption. Thickness of the Si NM: 1500 nm.

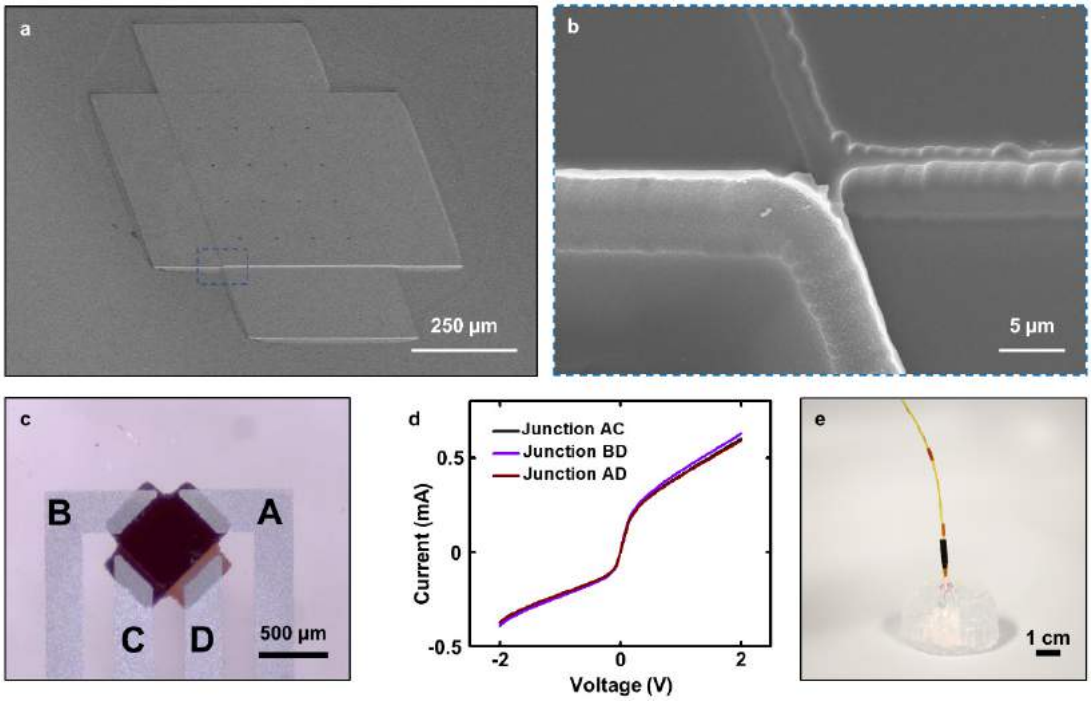

Supplementary Figure 6. Bioresorbable tri-color Si photodetector.

(a) Titled-view SEM image of the tri-color Si photodetector. (b) Enlarged view of a corner of the device to highlight the etched steps. (c) Top-down view of a tri-color Si photodetector. Electrodes of Zn are labeled A, B, C, and D in correspondence with the labels of doping layers in Figure 2a&b. (d) Measured I-V curves (at dark environment) between contacts of A and C, B and D, and A and D, respectively. n=6 independent experiments. (e) Image of a tri-color detector interfaced to a bioresorbable fiber optic probe, inserted into a brain model made of agarose hydrogel.

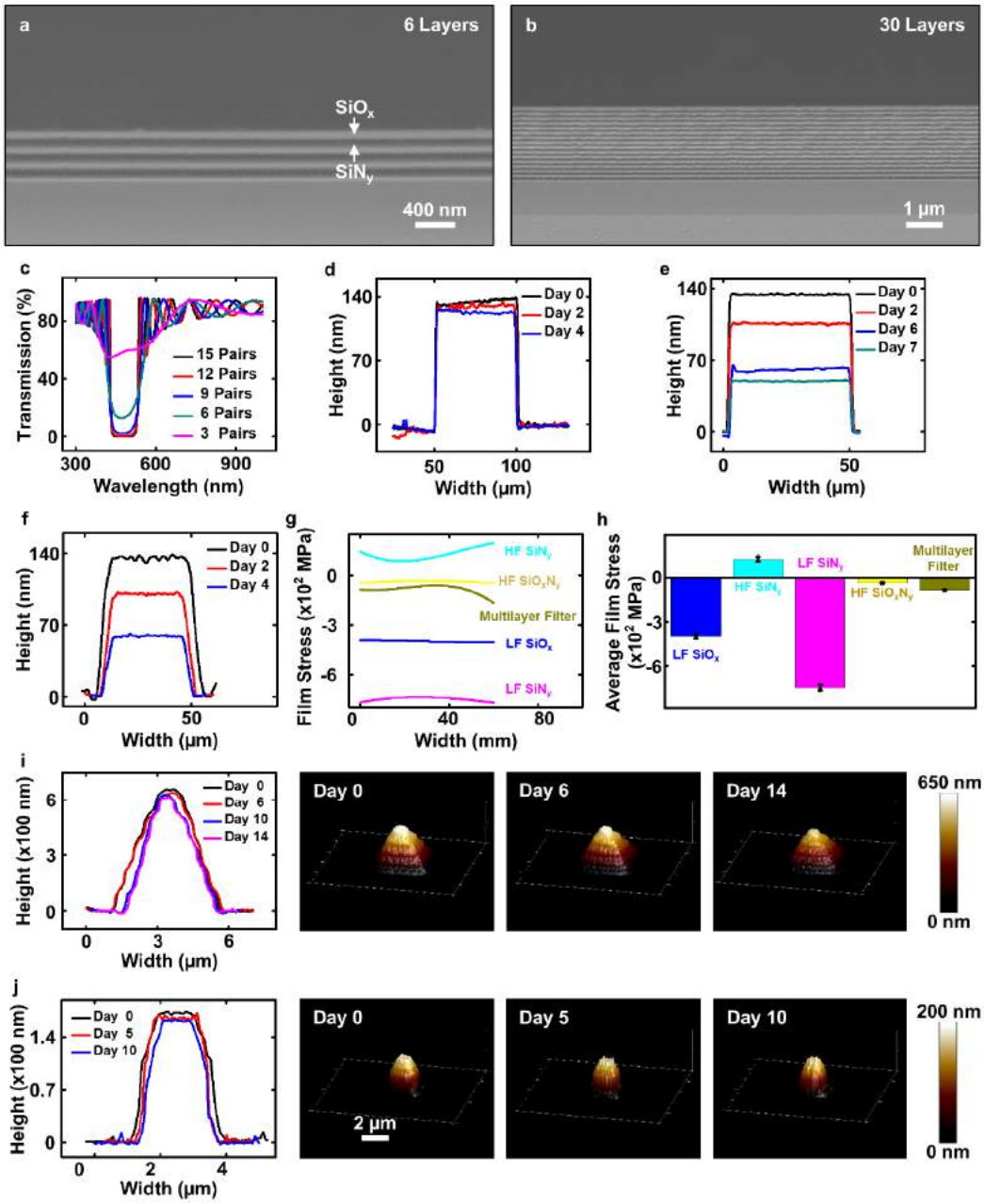

Supplementary Figure 7. Bioresorbable optical multilayer filters and the dissolution behaviors of multilayer assemblies of SiO_x and SiN_y thin films.

(a) Cross-sectional SEM images (90° tilted view) of a bioresorbable optical filter consisting of 3 pairs of SiO_x and SiN_y films with thicknesses of 54 nm and 85 nm, respectively. (b) Cross-sectional SEM images (90° tilted view) of a bioresorbable optical filter consisting of 15 pairs of SiO_x and SiN_y films with thicknesses of 54 nm and 85 nm, respectively. (c) Optical simulation of the transmission spectra of bioresorbable optical multilayer filters with numbers of pairs of SiO_x and SiN_y films between 3 and 15. (d) Height profiles of a pad of SiO_x produced by low-frequency (LF) plasma-enhanced chemical vapor deposition (PECVD) at various times after immersion in phosphate-buffered saline (pH=7.4) at 80 °C. (e)

Height profiles of a pad of SiN_y produced by high-frequency (HF) PECVD at various times after immersion in phosphate-buffered saline (pH=7.4) at 80 ^oC. (f) Height profiles of a pad of SiN_y produced by LF PECVD at various times after immersion in phosphate-buffered saline (pH=7.4) at 80 ^oC. (d), (e), and (f) are measured by profilometer. (g) Stress profiles of films of LF Si oxide, HF SiN_y, LF SiN_y, HF SiO_xN_y, and a multilayer filter of SiO_x and SiN_y. Positive, and negative stresses represent tensile and compressive stresses, respectively. (h) Average stresses for films of LF SiO_x, HF SiN_y, LF SiN_y, HF SiO_xN_y, and multilayer filter of SiO_x and SiN_y. (g) and (h) are measure by stylus profilers. (i) Profiles and AFM topographical images of a pad of a multilayer assembly of SiN_y and SiO_x at various stages of dissolution in phosphate-buffered saline (pH=5, via adding acetic acid) at 80 ^oC. (j) Profiles and AFM topographical images of a pad of SiO_xN_y at various times after immersion in phosphate-buffered saline (pH=7.4) at 80 ^oC. Deposition parameters for each film appear in Supplementary Note III. (a-j) n=3 independent experiments.

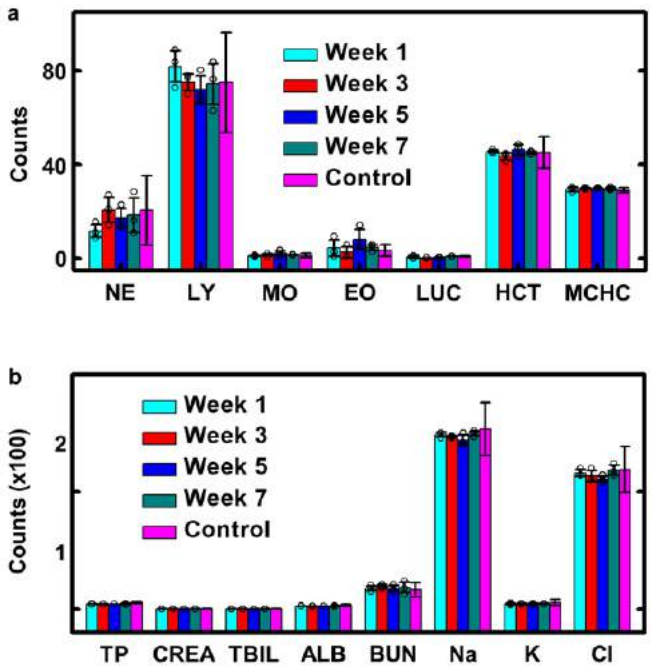

Supplementary Figure 8. Analysis of complete blood count (a) and blood chemistry (b) for the mice analyzed in Figure 3a&b.

Control data (labeled as Normal) is provided by the mice supplier (Charles River Laboratories). Abbreviations and corresponding units include, NE: percentage of neutrophils (%), LY: percentage of lymphocytes (%), MO: percentage of monocytes (%), EO: percentage of eosinophils (%), HCT: hematocrit (%), MCHC: mean corpuscular hemoglobin concentration (g/dL), LUC: percentage of large unstained cells (%), TP: total protein (g/dL), CREA: creatinine (mg/dL), TBIL: total bilirubin level (mg/dL), ALB: albumin (g/dL), BUN: blood urea nitrogen (mg/dL), Na: sodium (mEq/L), K: potassium (mEq/L), Cl: chloride (mEq/L). (a-b) n= 12 biologically independent mice. Results are shown as means ± s.e.m..

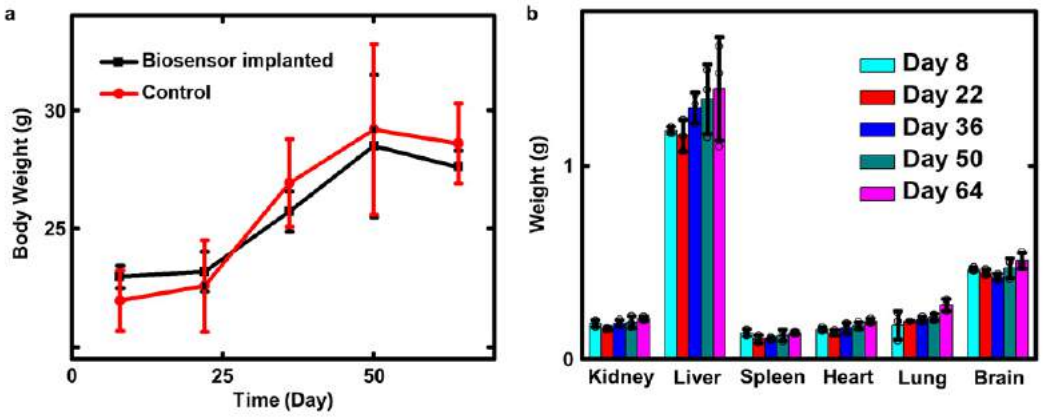

Supplementary Figure 9. Weights of the bodies and the key organs of mice implanted with a bioresorbable device for spectroscopic tissue characterization.

(a) Changes in body weights of mice implanted with bioresorbable devices for spectroscopic tissue characterization (for each data point, number of biologically independent mice used, n = 3) compared with control animals (n = 3). (b) Changes in weights of key organs (kidney, liver, spleen, heart, lung, brain) of mice implanted with bioresorbable devices for spectroscopic tissue characterization (for each time point, number of biologically independent mice used, n=3). (a-b) Results are shown as means ± s.e.m..

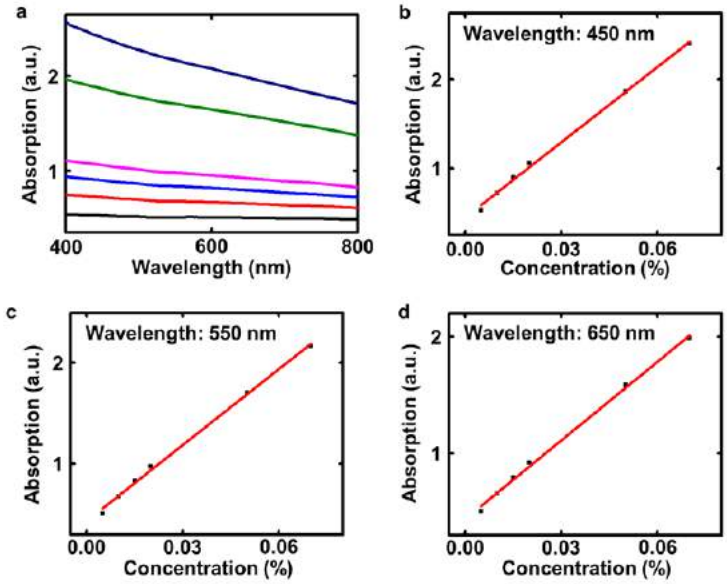

Supplementary Figure 10. In vitro measurements of melanin concentration in phosphate-buffered saline performed with a bioresorbable devices for spectroscopic tissue characterization.

(a) Spectral measurements performed on melanin solutions with various concentrations relevant to typical levels found in humans, using a bioresorbable Si NM photodetector coupled to a bioresorbable fiber optic probe. A tunable laser injects, through a PLGA fiber into solution, monochromatic light with wavelength between 400 nm and 800 nm. A Si NM photodetector located at the tip of the sensor generates electrical signals in response to transmitted light at each corresponding wavelength. Calibration curves corresponding to responses at 450 nm (b), 550 nm (c), and 650 nm (d) measured in vitro. All the calibration curves indicate linear responses to concentration of melanin. (a-d) n=3 independent experiments.

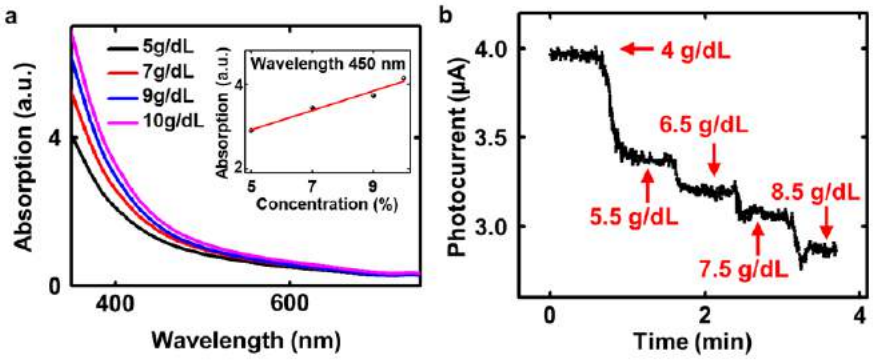

Supplementary Figure 11. In vitro measurements of albumin concentration in phosphate-buffered saline performed with a bioresorbable devices for spectroscopic tissue characterization.

(a) Spectral measurements performed on albumin solutions with various concentrations between 5 g/dL and 10 g/dL, relevant to typical levels found in humans, using a bioresorbable Si NM photodetector coupled to a bioresorbable fiber optic probe. The wavelength range spans 350 nm to 800 nm. Inset: calibration curves corresponding to responses at 450 nm measured in vitro. (b) Measurements for in phosphate-buffered saline with solutions of albumin added at different time points. The step-like profile of the measured photocurrent is consistent with events of adding albumin solution. Light wavelength: 633 nm. (a-b) n=3 independent experiments.

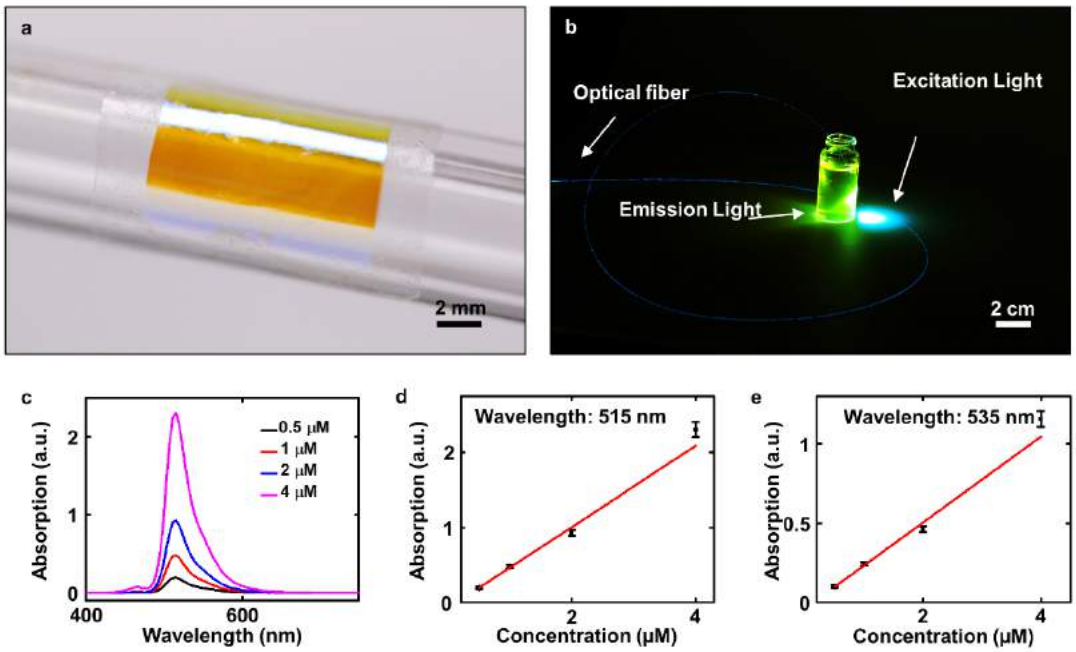

Supplementary Figure 12. Bioresorbable probe for spectroscopic characterization integrated with a bioresorbable optical filter and in vitro measurements of calcium concentration by fluorescence sensing.

(a) Image of a bioresorbable optical multilayer filter wrapped on a glass rod with diameter 8 mm. The filter consists of 15 pairs of SiO_x and SiN_y films with thicknesses of 54 nm and 85 nm, respectively, encapsulated by a 10-μm thick film of PLGA. (b) Experimental setup for in vitro measurements of calcium concentration using a device that incorporates such a filter. (c) In vitro measurements of absorption spectra of solutions of calcein and calcium at pH =13. Concentration of calcein: 2.5 μM, concentration of calcium ranges from 0.5 μM to 4 μM. (d), (e) Calibration curves corresponding to measurements at 515 nm (d) and 535 nm (e). (c-e) n=3 independent experiments.

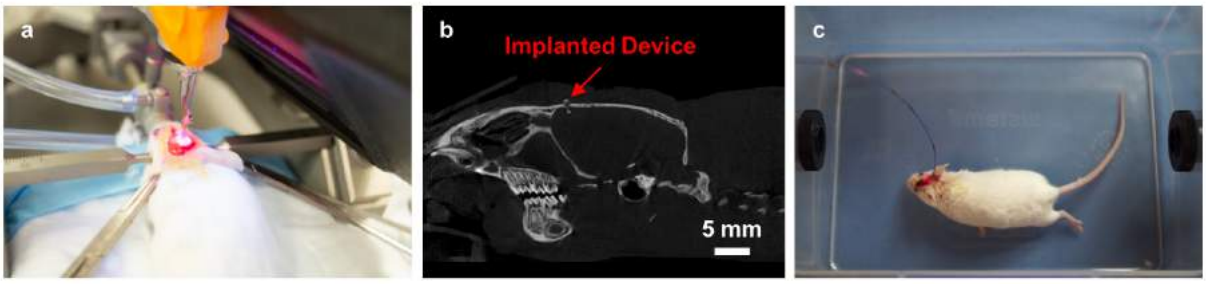

Supplementary Figure 13. Surgical implantation of a bioresorbable photodetector coupled to a bioresorbable fiber optic probe into a cerebral region near parietal lobe.

(a) Image of insertion of a device into the brain after performing a craniotomy procedure. (b) Sagittal-view image obtained by computed tomography form a mouse with an implanted device. n=3 biologically independent mice. (c) Image of a freely-moving mouse implanted with a device for continuous measurements of cerebral oxygenation.

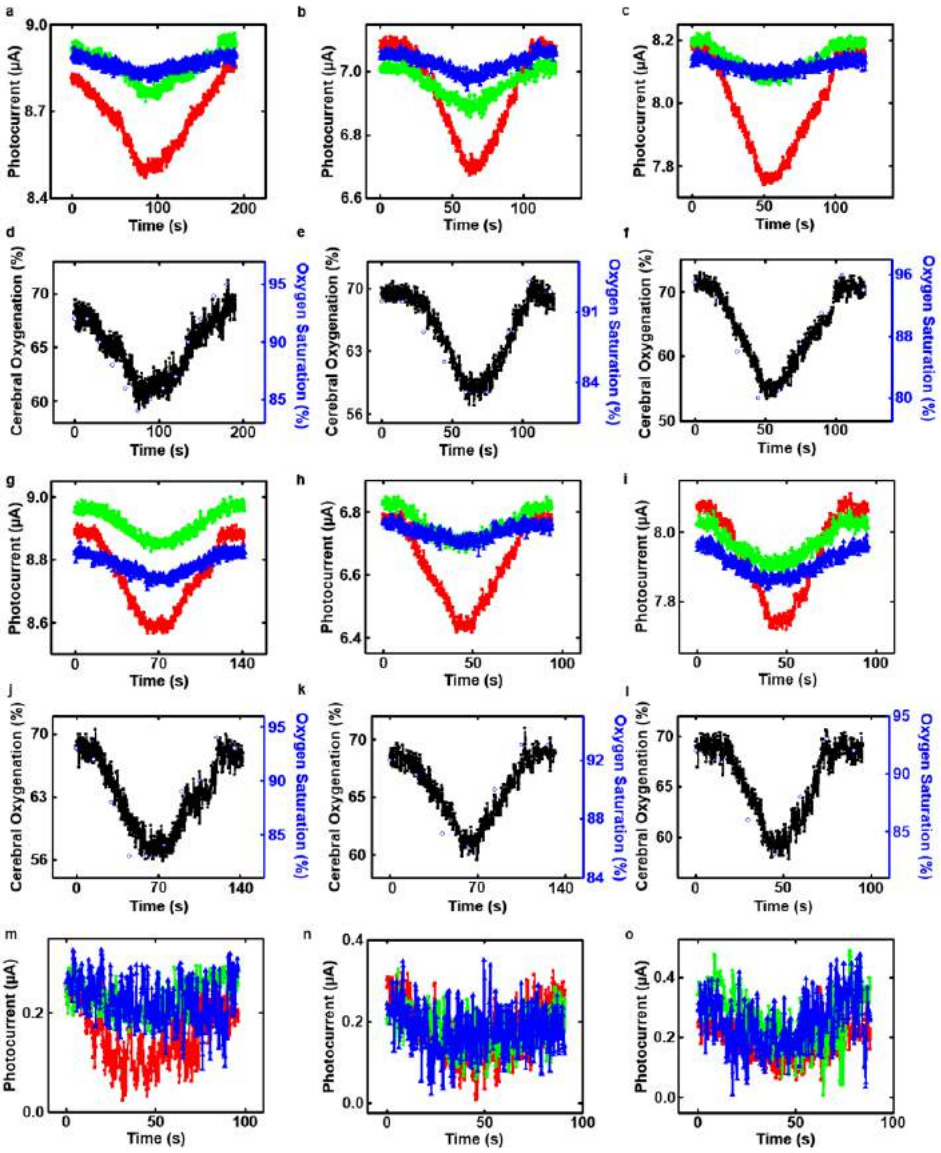

Supplementary Figure 14. Monitoring cerebral oxygenation in three biologically independent mice via spectroscopic measurements using bioresorbable optical probes.

(a-c), (g-i) and (m-o) Measured photocurrents from junction AB, BC, and CD of a tri-color photodetector based bioresorbable spectrometer implanted into the cerebral region near the parietal lobe. (d-f) and (j-l) Cerebral oxygenation calibrated based on measurements of implanted bioresorbable spectrometer, and blood oxygen saturation measured by a commercial sensor placed at the hind paw of the mice. (a-f), (g-l), and (m-o) are measured on day 1, day 7, and day 10, respectively, after implantation. (a), (d), (g), (j), and (m) are from mouse 1; (b), (e), (h), (k), and (n) are from mouse 2; (c), (f), (i), (l), and (o) are from mouse 3. The sensitivity (based on comparison of an average measured value with baseline noise) and accuracy (based on comparison of a measured value with that of a commercial medical tool, PhysioSuite for Mice & Rats, Kent Scientific) on day 1 are 2.9 % and 4.3 %, respectively. The sensitivity and accuracy on day 7 are 3.2 % and 4.7 %, respectively. (a-o) n=3 independent experiments.

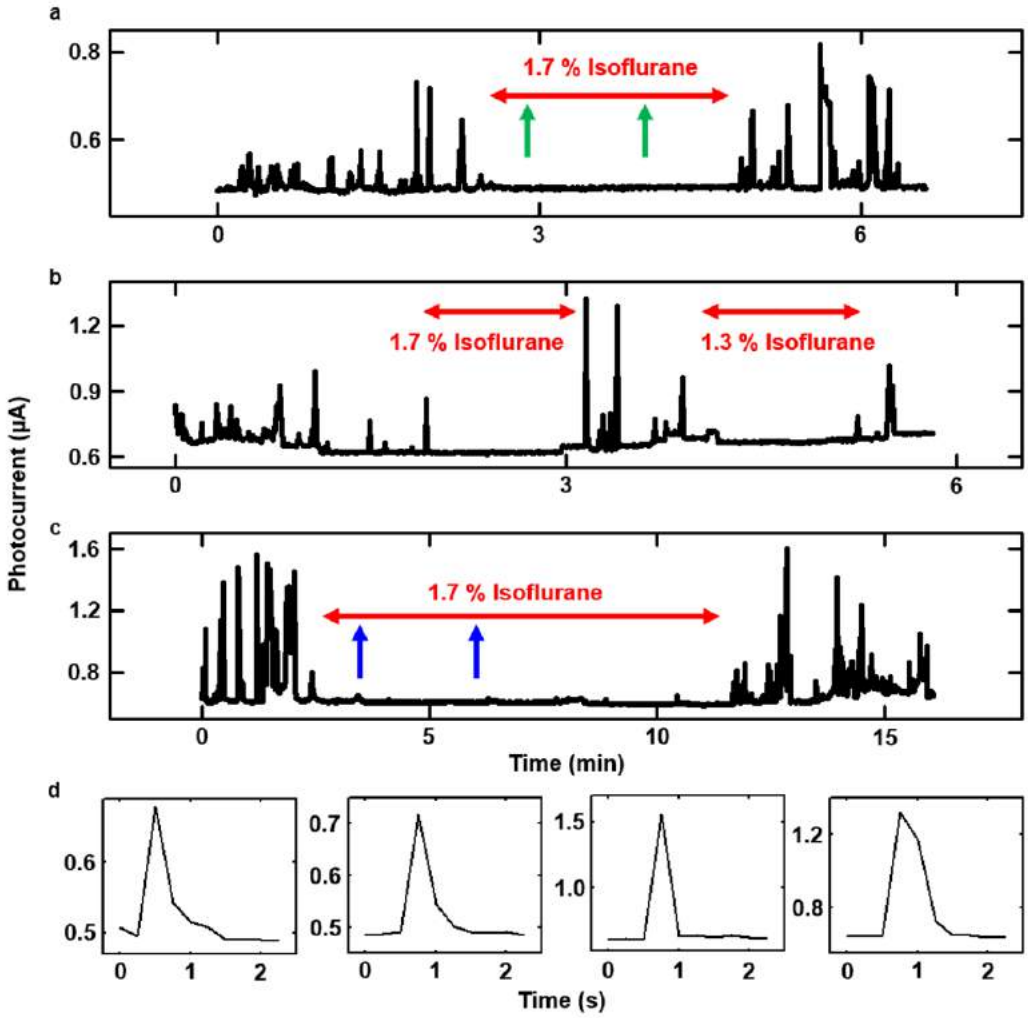

Supplementary Figure 15. Measured photocurrent from implanted bioresorbable optical probes in response to fluorescence (Oregon Green 488 BAPTA-2, AM) modulated by neural calcium transients.

(a), (b), and (c) are measured from three biologically independent mice, respectively. Anesthetic inductions (indicated by red horizontal double arrows) using isoflurane effectively suppress events of neuronal signaling. (a) Shaking (at the times indicated by green vertical arrows) the connecting wires of the implanted bioresorbable optical probes have little effect on measurements of neural activity. (c) Poking (at the times indicated by blue vertical arrows) the backs of mice with implanted devices show little effect on measurements of neural activity. (d) Representative plots of single spikes of the Ca2+ fluorescence recordings. n=4 independent experiments.

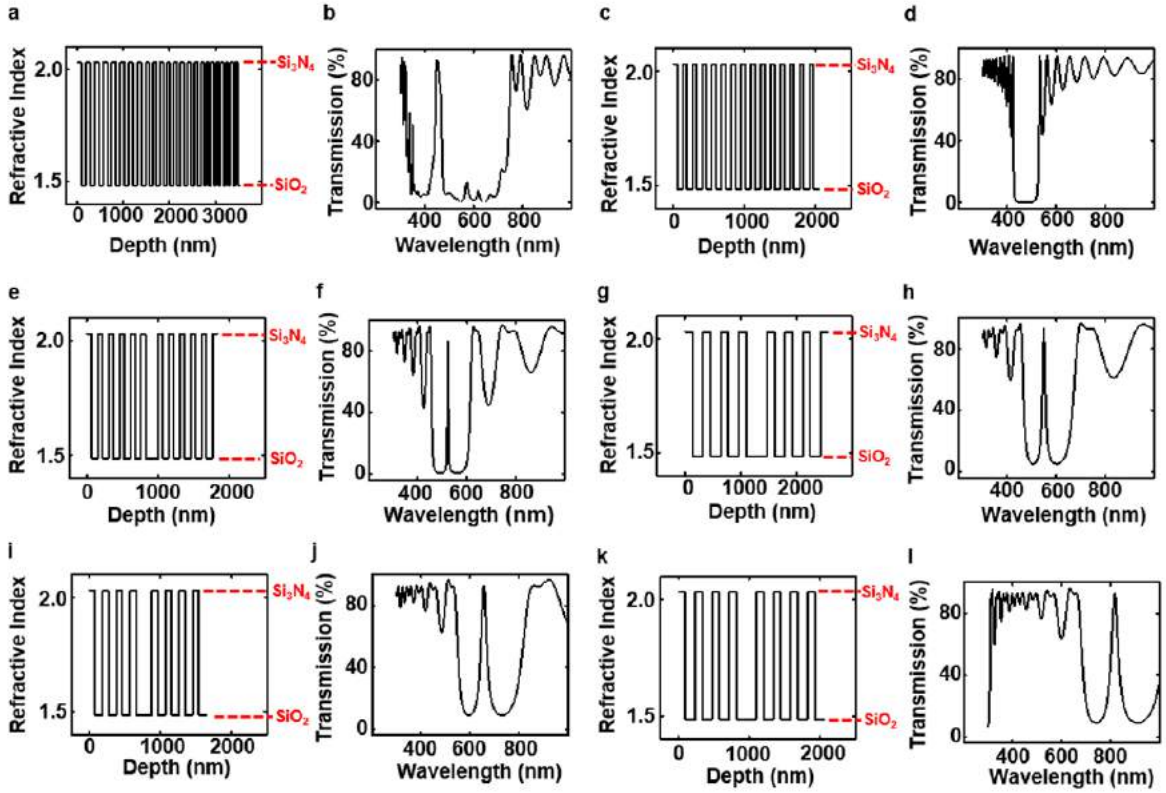

Supplementary Figure 16. Bioresorbable optical filters based on multilayer assemblies of films of SiO_x and SiN_y.

The measured transmission spectra of multilayer assemblies of films of SiO_x and SiN_y with depth profiles of refractive index (a), (c), (e), (g), (i), and (k), are shown in (b), (d), (f), (h), (j), and (l), respectively. (b), (f), (h), (j), and (l) exhibit narrow-band transmission windows at wavelengths of 503 nm, 525 nm, 550 nm, 650 nm, and 833 nm, respectively. (d) shows a band-block filter with blocking wavelength range from 430 nm to 520 nm. (a-l) n=3 independent experiments.

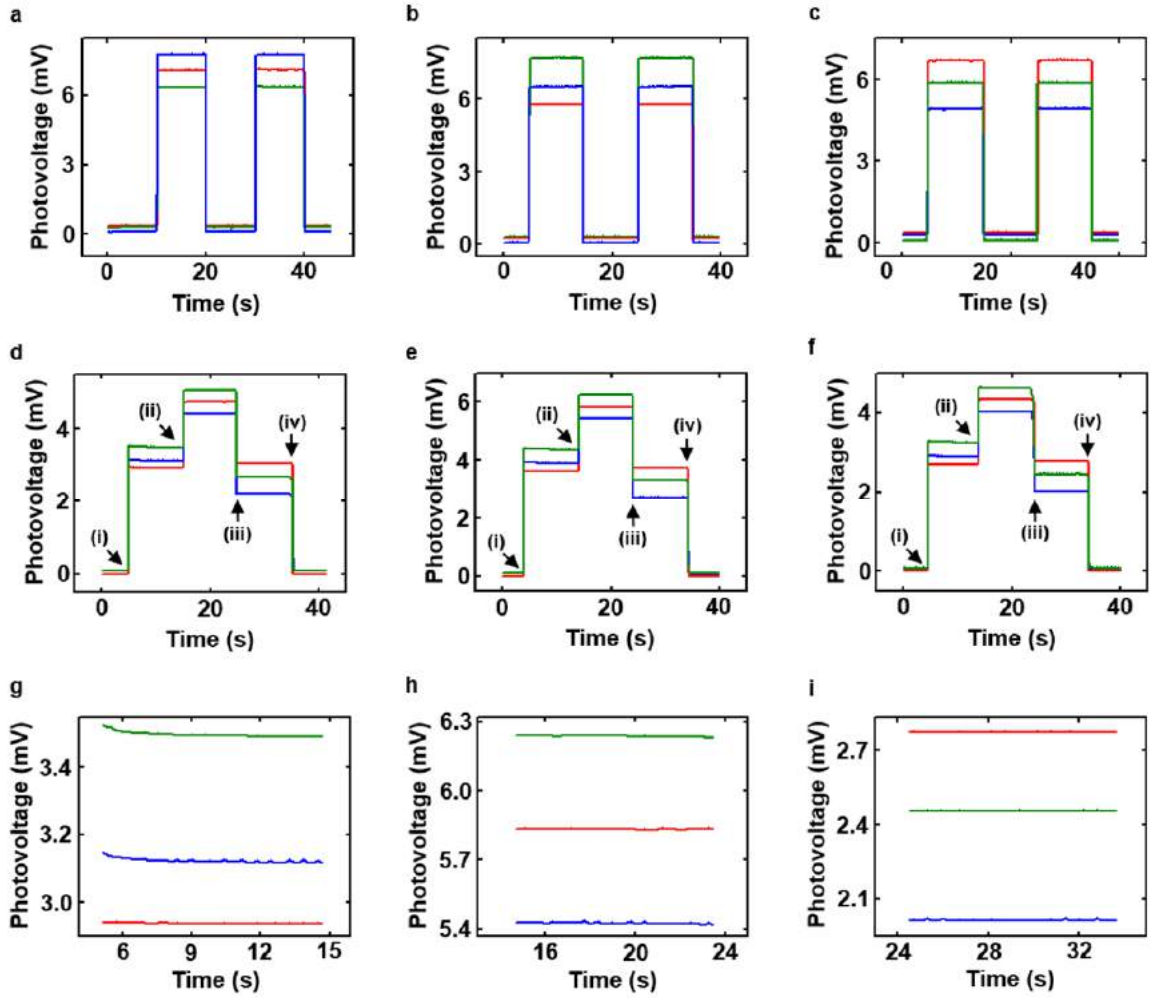

Supplementary Figure 17. Measured photovoltages generated from junction AB (blue line), BC (green line), and CD (red line) as functions of time under square-wave illumination.

Measurements are collected from three different tri-color Si photodetectors: (a), (d), (g) are from the first one; (b), (e), (h) are from the second one; (c), (f), (i) are from the third one. (a), (b), and (c) are photovoltaic responses to square-wave illumination with white light (broad-band wavelength), green light (wavelength 530 nm), and red light (wavelength 633 nm), respectively. (d), (e), and (f) are photovoltaic responses to illumination with green and red light in a programmed sequential combination, where (i) green light on, red light off; (ii) green light on, red light on; (iii) green light off, red light on; (iv) green light off, red light off. (g): an enlarged view of stage (i) of (d). (h): an enlarged view of stage (ii) of (e). (i): an enlarged view of stage (iii) of (f). (g), (h), and (i) show low levels of noise compared to the measured signals.

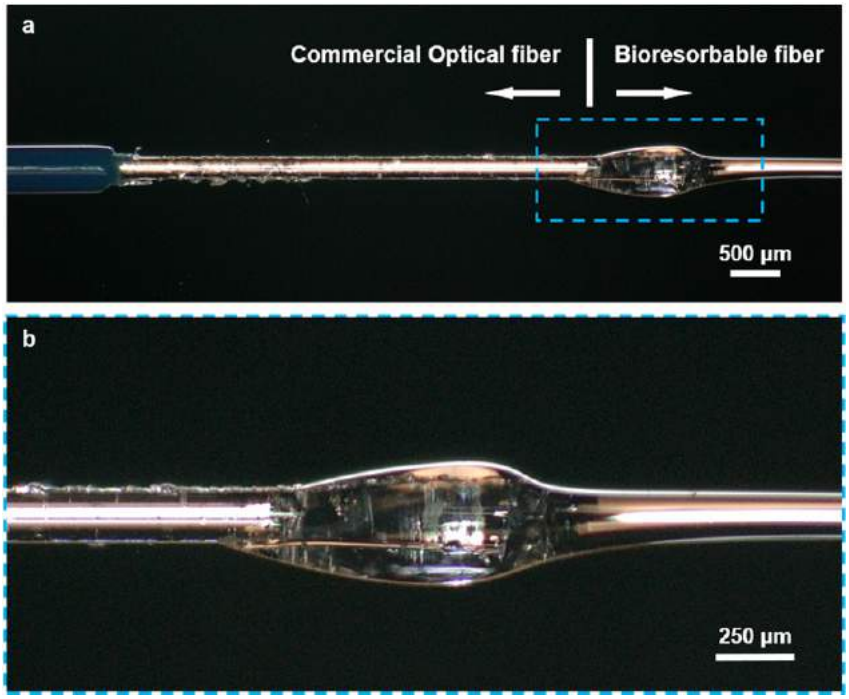

Supplementary Figure 18. Coupling between commercial optical fiber and bioresorbable fiber.

Using the tip of a commercial optical fiber as a lead to draw a bioresorbable fiber from a preform of poly(lactic-co-glycolic acid) (PLGA) at a temperature 200 ^{o}C naturally couples the resulting bioresorbable fiber to the commercial fiber, as a means to connect to the external broad-band light source. (a) microscope image of the coupling region between a commercial fiber and a bioresorbable fiber. n=6 independent experiments. (b) enlarged view of the coupling interface.

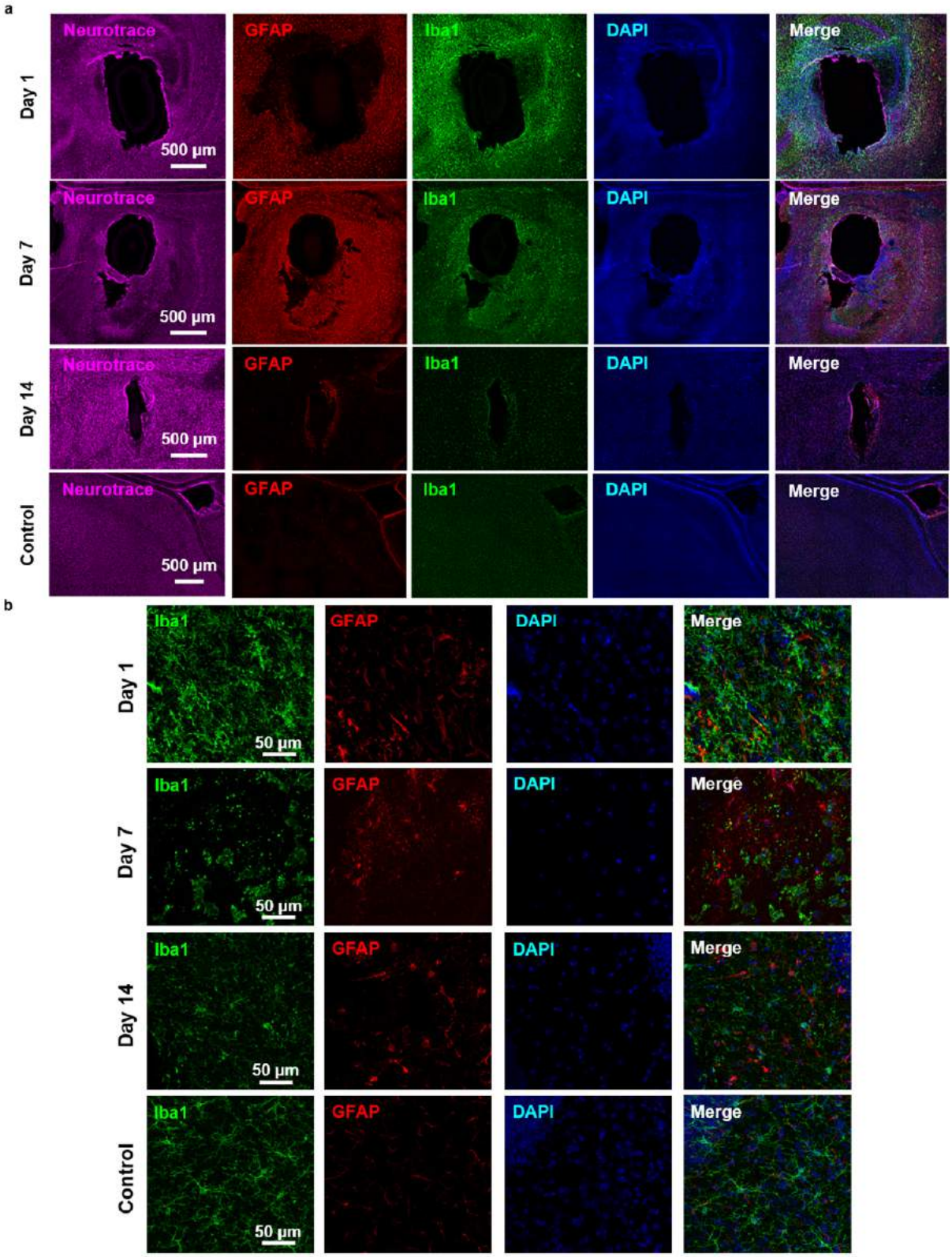
a
Day 1
Day 7
Day 14
Control
Neurotrace
GFAP
Iba1
DAPI
Merge
500 µm
b
50 µm

Supplementary Figure 19. Representative confocal images of 30 μm horizontal striatal slices at various stages after implantation of the bioresorbable optical probes (collected on day 1, 7, and 14, covering a typical lifetime of the bioresorbable device) with comparisons to a control group.

The images show immunohistochemical staining for Nissl bodies (neurotrace, purple), astrocytes (GFAP, red), activated microglia (Iba1, green), DNA (DAPI, blue), and overall lesion from bioresorbable optical probes. (a) Cross-sectional view of the implantation site. n=3 independent experiments. (b) enlarged view of regions in the vicinity of the probes. All histological and confocal settings were kept consistent across groups. Scale bars are consistent for each group, defined as Day 1, Day 7, Day 14, and Control.

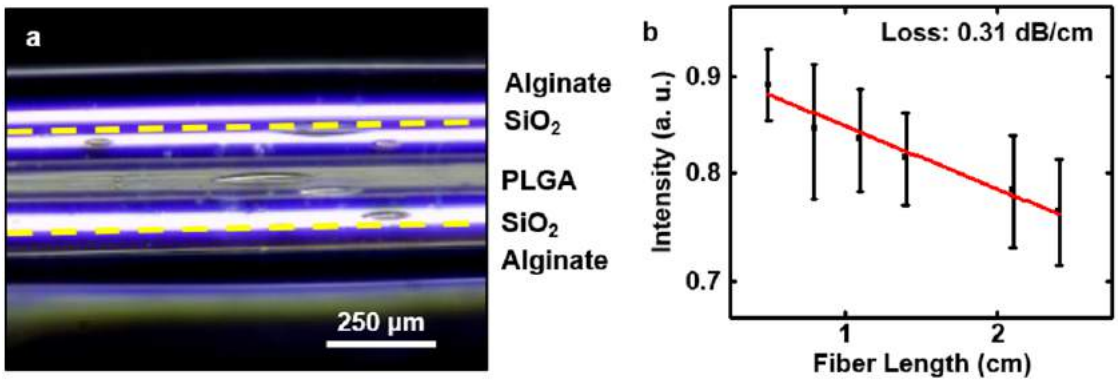

Supplementary Figure 20. Bioresorbable optical fiber with PLGA as core, SiO2 (thickness ~ 200 nm) as a first cladding, and Alginate hydrogel (thickness ~ 150 µm) as a second cladding.

(a) Microscope image of the bioresorbable optical fiber. n=6 independent experiments. (b) Measured transmission intensity for a bioresorbable optical fiber in chicken tissue, as a function of fiber length. The measurements indicate a decreased propagation loss (~ 0.31 dB/cm) for the multi-clad bioresorbable fiber, compared with core-only PLGA fiber (propagation loss 1.59 dB/cm) or alginate-clad PLGA fiber (0.77 dB/cm) (Supplementary figure S1). n=6 independent experiments. Results are shown as means ± s.e.m..

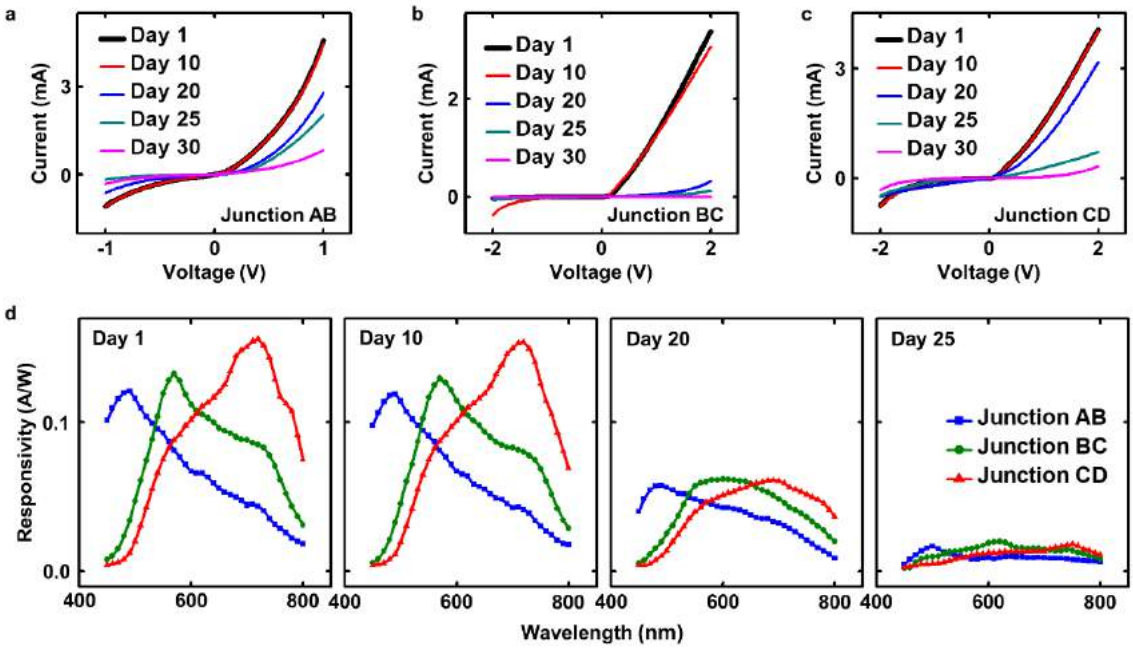

Supplementary Figure 21. Performance characteristics of a tri-color silicon photodetector at various stages of immersion in phosphate-buffered saline at 37 °C.

(a-c) Measured I-V characteristics (at dark environment) of a tri-color silicon photodetector on day 1, 10, 20, 25, and 30, after immersion in phosphate-buffered saline at 37 °C. (a) measurements of junction AB, (b) measurements of junction BC, (c) measurements of junction CD. (d) Photoresponses of junctions AB (blue line), BC (green line), and CD (red line) as a function of illumination wavelength. Measurements were carried out on day 1, 10, 20, and 25 after immersion in phosphate-buffered saline at 37 °C. (a-d) n=3 independent experiments.

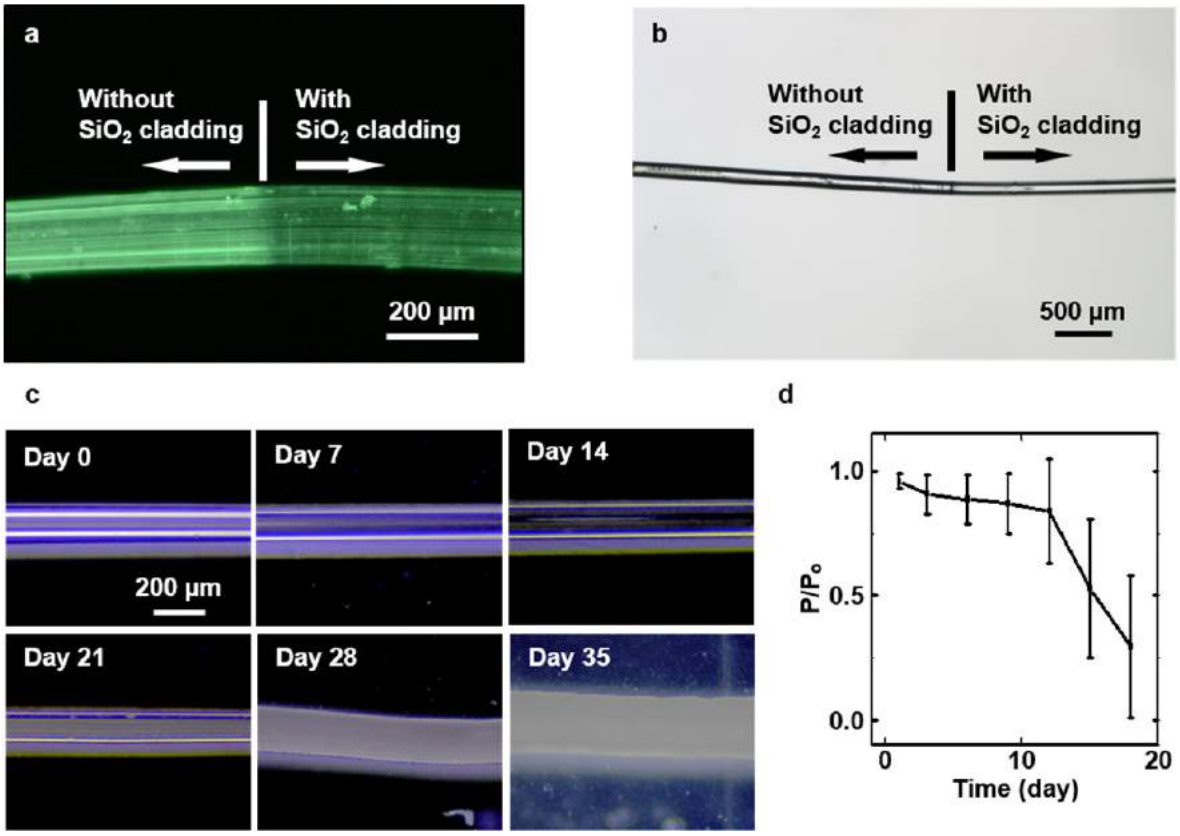

Supplementary Figure 22. Bioresorbable fiber with PLGA (diameter 200 µm) as core and SiO_2 as cladding.

(a) Microscope image shows the bioresorbable fiber with transmission of green light (570 nm). (b) Microscope image of the bioresorbable fiber. (c) Microscope images of the bioresorbable fiber collected at various stages of immersion in phosphate-buffered saline (PBS) at 37^{o}C. The measured functional lifetime of the bioresorbable fiber is around 10 days, with propagation loss stabilized at 0.5±0.1 dB/cm. Significant swelling of the fiber was observed on day 28. (a-c) n=6 independent experiments. (d) Measurements of optical attenuation of the fiber (PLGA core, and SiO_2 cladding) during immersion in PBS at 37 ^{o}C. P: measured output light intensity. Po: the highest measured output light intensity on day 1. n=6 independent experiments. Results are shown as means ± s.e.m..

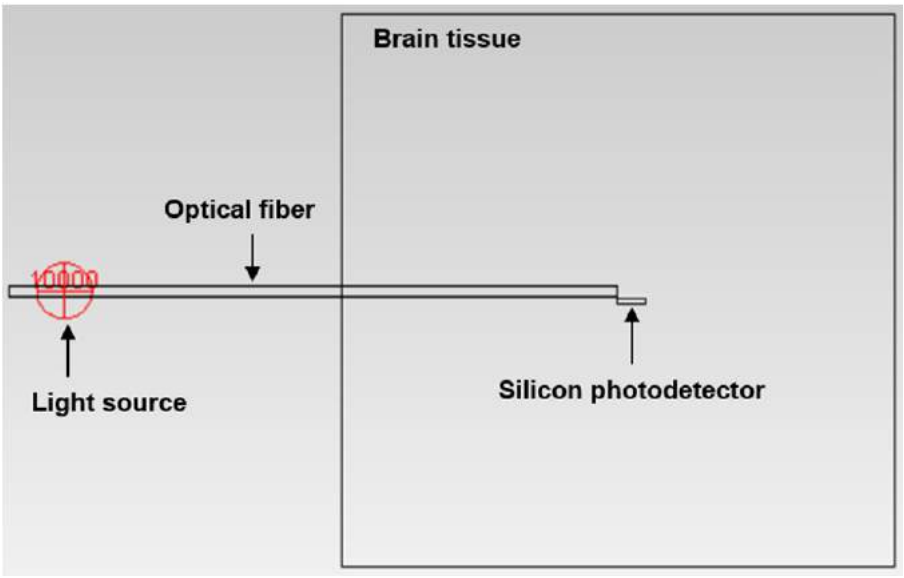

Supplementary Figure 23. Simulation model to analyze the light detected by the silicon photodetector of the bioresorbable optical probe (as shown Figure 1).

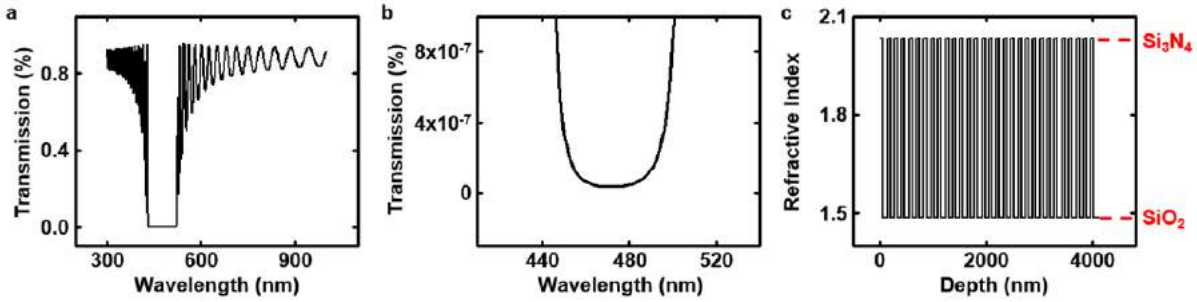

Supplementary Figure 24. Bioresorbable optical filter based on 60-layer assemblies of films of SiO_x and SiN_y.

(a) Measured transmission spectrum of the optical filter at 0^o incidence angle. (b) an enlarged (410 nm – 540 nm) view of the transmission spectrum near the band-stop regime (450 nm to 520 nm). (c) Depth profile of the refractive index for the 60-layer filter. (a-c) n=3 independent experiments.

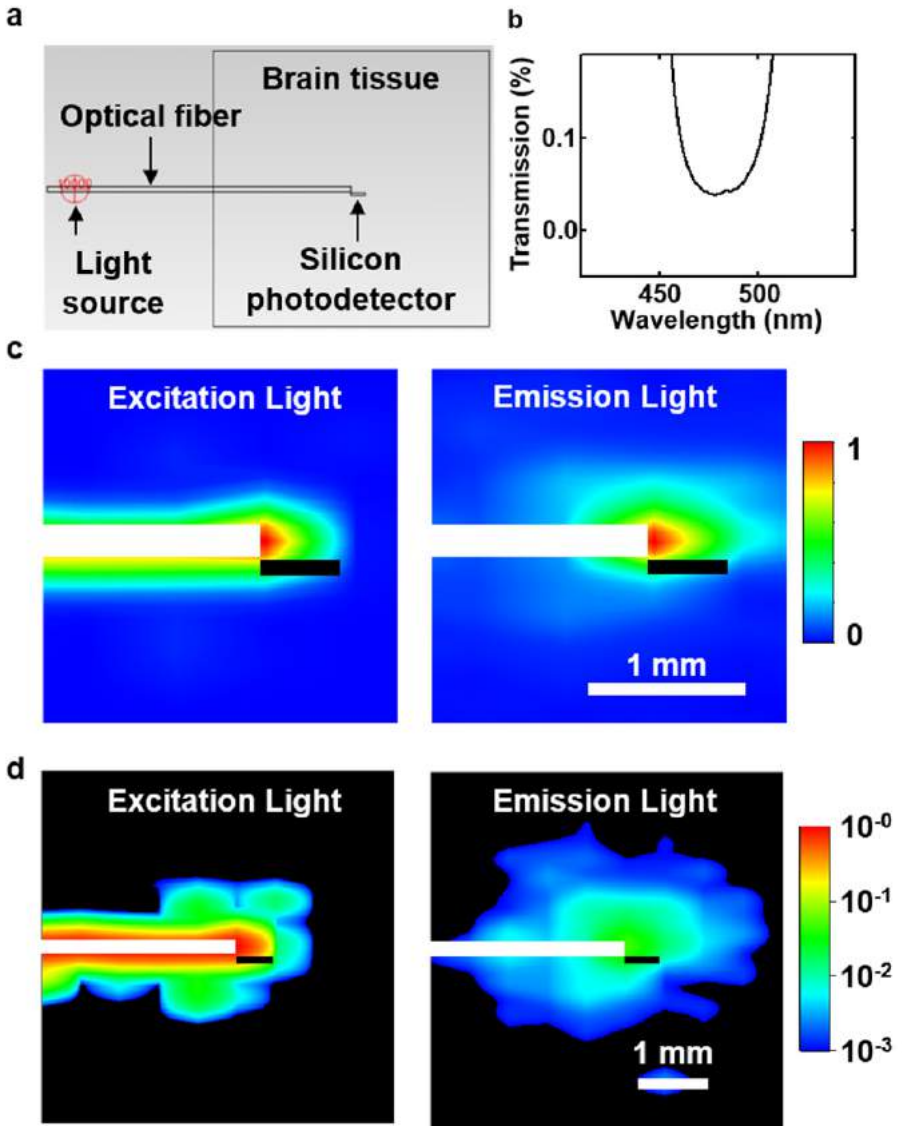

Supplementary Figure 25. Simulation model to determine measurements of fluorescence using the bioresorbable optical probe.

(a) Schematic illustration of the simulation model of fluorescence sensing using the bioresorbable optical probe. The dye is filled in a spherical area with a radius of 2 mm and a concentration of 2 μM. (b) an enlarged (410 nm – 550 nm) view of the transmission spectrum near the band-stop regime (450 nm to 520 nm) of the optical filter shown in Figure 3. The optical density is around 3.52. (c) Normalized intensity profile of excitation light delivered through the bioresorbable optical fiber (Left), and emission light generated from fluorescence-stained brain tissue (Right). (d) Profile of light intensity relative to that of the light source for excitation light delivered through the bioresorbable optical fiber (Left), and for emission light generated from fluorescence-stained brain tissue (Right). (c-d) n=3 independent experiments. Color bar represents quantitative intensity of light with arbitrary unit.

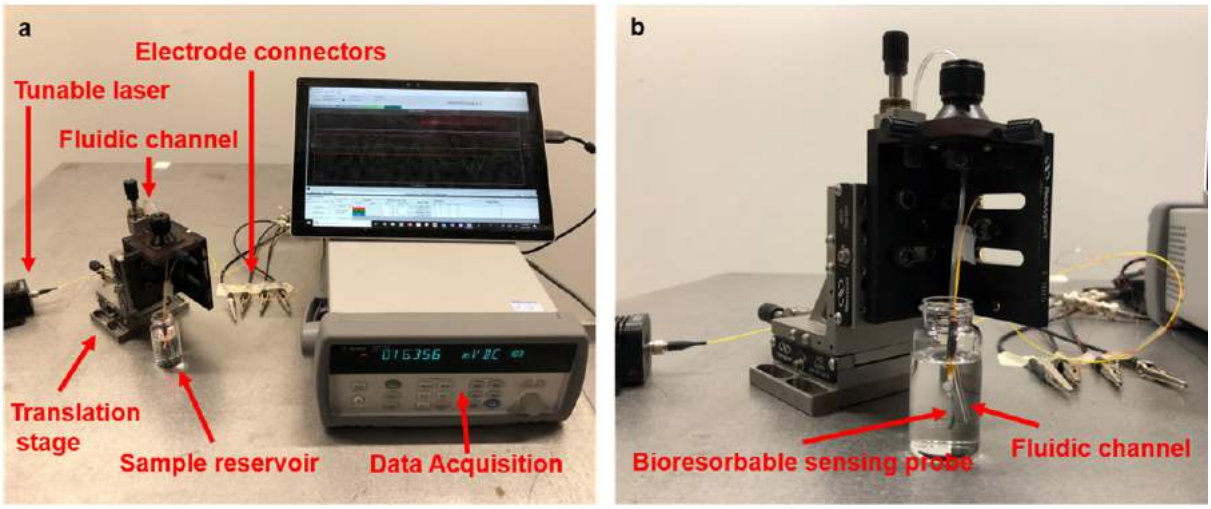

Supplementary Figure 26. Optical setup for the in vitro measurements of Figure 5.

(a) The setup includes: 1) a tunable laser (NKT photonics supercontinuum laser, integrated with SuperK VARIA tunable single line filter) which generates light of a single wavelength, multiple wavelengths, or a range of wavelengths; 2) a commercial fiber which connects to the PLGA fiber and delivers light to the bioresorbable sensing probe; 3) a data acquisition system (Keysight Technologies 347970A) that connects to a computer and records electrical measurements of multiple electrical channels; 4) 4 electrode connectors that connects the electrodes of bioresorbable sensing probe with the data acquisition system; 5) a sample reservoir that contains blood sample for oxygenation measurement (Figure 5a&b) and for melanin measurement (Figure 5c&d), or Calcein solution for measurement of calcium concentration (Figure 5f-h); 6) a fluidic channel that enable a controlled flow of sodium dithionite dissolved in blood for oxygenation measurement, or melanin dissolved in phosphate-buffered saline (PBS) for melanin measurements, or calcium chloride dissolved in phosphate-buffered saline (PBS) for measurement of calcium concentration; 7) a translation stage that stabilizes the position of the bioresorbable sensing probe inside sample reservoir. The temperature measurement follows a similar setup except that the fluidic channel is replaced with a thermocouple and a heating stage is added underneath the sample reservoir. The optical power used for the in vitro measurement is around 0.7 mW. (b) an enlarged view of sample reservoir to show the bioresorbable sensing probe and the fluid channel.